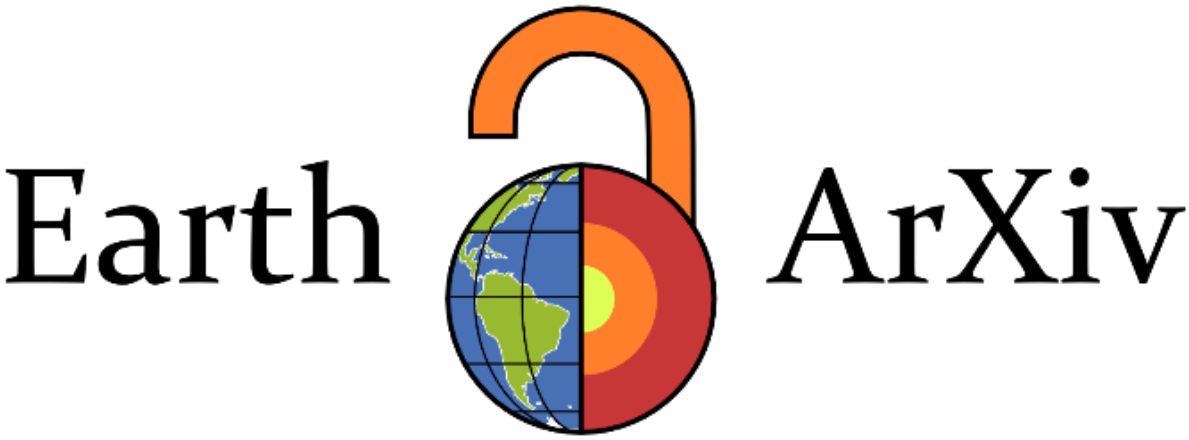

ORIGINAL ARTICLE

Error-aware surrogate modeling for accelerated three-dimensional probabilistic inversion of controlled-source electromagnetic data

Short title: Error-aware 3D CSEM probabilistic inversion

Matías W. Elías[1,2] | Marina Rosas-Carbajal[3] | Federico Späth[4] | Fabio I. Zyserman[1,2]

[1]Centro de Investigaciones Geofísicas, Facultad de Ciencias Astronómicas y Geofísicas, Universidad Nacional de La Plata, Argentina

[2]Consejo Nacional de Investigaciones Científicas y Técnicas (CONICET), Argentina

[3]Institut de Physique du Globe de Paris, CNRS, Université Paris Cité, 1 rue Jussieu, Paris, 75005, France

[4] YPF S.A., Buenos Aires, Argentina

Correspondence

M. W. Elías, La Plata, Buenos Aires, Argentina

Email: melias@fcaglp.unlp.edu.ar

Funding information

CONICET through grant PIP 11220200101056CO.

We present a workflow for three-dimensional probabilistic inversion of controlled-source electromagnetic data that effectively balances accuracy and computational efficiency. The approach mitigates the high computational cost of forward modeling by employing a surrogate model derived from a mesh coarsening strategy. To account for the modeling errors inherent to this approximation, we implement a deep-learning–based parametric correction, enabling the joint inversion of correction and subsurface physical parameters. We use a synthetic marine experiment to verify that the proposed method recovers the true subsurface parameters.

The inclusion of an error correction significantly improves predictive accuracy and reduces computation time compared to conventional forward modeling. Application to a real world marine data acquisition further illustrates the capability of the method to estimate the geometry and location of an oil reservoir. Our results highlight the potential of deep-learning–assisted surrogate modeling as a practical tool for accelerating the probabilistic inversion.

KEYWORDS

inversion, electromagnetics, resistivity, reservoir geophysics

Acknowledgments

Numerical computations were performed on the S-CAPAD/DANTE platform, IPGP, France. We thank YPF S.A. for providing the field data for this study, and Dr. Eric Laloy and Dr. Shiran Levy for making publicly available the implementation the GAN-based probabilistic inversion approach and its extension for model errors using the Spatial-GAN.

Data availability

The synthetic data produced in this study, as well as the proprietary and third-party software (publicly available) adapted for this work, are available from the corresponding author upon reasonable request (e-mail: melias@fcaglp.unlp.edu.ar). The field data used in this study were provided by YPF S.A. under license and cannot be shared by the authors.

1 | INTRODUCTION

The Controlled-Source Electro-Magnetic method (CSEM) is a well-established and mature technique in geophysical research. It is used to determine the distribution of electrical conductivity in the subsurface, which strongly depends on temperature, mineralogical composition, porosity, and pore fluid content of the constituent rocks (Ward & Hohmann, 1987). In turn, they allow the identification of subsurface structures in a range of a few meters to tens of kilometers depth. Their noninvasive nature and cost-effective implementation has motivated their application for diverse purposes, such as geothermal reservoirs characterization (e.g. Coppo et al., 2016; Darnet et al., 2020; Castillo-Reyes et al., 2021), monitoring of CO_2 storage reservoirs (e.g. Grayver et al., 2014; Streich, 2016; Puzyrev, 2019; Tveit et al., 2020), oil and gas resource exploration in marine environments (e.g. Dunham et al., 2018; Schaller et al., 2017; Ettayebi et al., 2023; Thorkildsen & Gelius, 2023), study of hydrothermal systems in volcanic areas (e.g. Barker, 2004; Hölz et al., 2015; Ishizu et al., 2024), groundwater exploration (e.g. Gustafson et al., 2019; Ishizu & Ogawa, 2021), gas hydrate reservoirs detection (e.g. Schwalenberg et al., 2017; Attias et al., 2018), and mineral exploration (e.g. Gehrmann et al., 2019; Mörbe, 2020).

Geophysical inversion involves inferring remote subsurface properties and structures by combining observable data and the application of physical theories. In particular, the Electro-Magnetic (EM) data inversion allows for obtaining information about the spatial distribution of the subsurface electrical conductivity. For this purpose, the study region is subject to spatial (and, if necessary, temporal) parameterization of the distribution of the physical properties of interest (Blatter et al., 2021). It is well established that multiple physical descriptions (models) can equally explain the observed geophysical data (Menke, 1989). The solution of the inverse EM problem is characterized by non-uniqueness and instability mainly due to incomplete data coverage, errors in measurements and modeling. Deterministic approaches to solve the inverse problem are formulated as optimization problems solved iteratively through regularization and linearization (Menke, 1989). These methods are computationally efficient in searching for a single model that adequately fits the data under a predefined model regularization. However, they lack a formal framework to quantify model uncertainty and to characterize the resolution of the inverted parameters (e.g. Rosas-Carbajal et al., 2015; Ray & Myer, 2019; Peng et al., 2024). In contrast, the Bayesian approach treats the inverse problem solution as a random

variable rather than a single deterministic model. Its aim is to infer a posterior probability density function (pdf) of the model parameters (Mosegaard & Tarantola, 1995). In this way, it provides a framework that explicitly accounts for observations, model parameters, and model uncertainty. Accounting for model uncertainty enables to define statistically justified constraints on the physical properties of interest (e.g. De Pasquale & Linde, 2017; Blatter et al., 2021).

Significant advances have been made in the probabilistic inversion of EM data in one-dimensional, two-dimensional (2D), and three-dimensional (3D), in magnetotelluric applications (e.g. Rosas-Carbajal et al., 2013, 2015; Manassero et al., 2020; Seillé & Visser, 2020; Blatter et al., 2021; Yao et al., 2023; Peng et al., 2024; Bajpai et al., 2025), and also in CSEM (e.g. Gehrmann et al., 2015; Penz et al., 2017; Ray & Myer, 2019; Blatter et al., 2019; Ray, 2021; Faghih et al., 2024). These works emphasize the high computational demand, primarily driven by the large number of forward model evaluations (10^5–10^6) required to ensure convergence. To optimize the computation time, is is important to use efficient posterior sampling strategies and fast forward-computations, along with careful parameterization of the problem. Markov chain Monte Carlo (MCMC) remains one of the most widely used methods for sampling the posterior distribution due to its conceptual simplicity (Peng et al., 2024), although it tends to be inefficient when applied to highly nonlinear, non-unique, and high-dimensional problems (e.g. Rosas-Carbajal et al., 2013). To address these limitations, several variants have been developed to improve sampling efficiency. For instance, Hamiltonian Monte Carlo methods incorporate gradient information from the posterior distribution to efficiently explore the parameter space (Neal, 2011; Peng et al., 2024), while adaptive approaches such as the Differential Evolution Adaptive Metropolis (DREAM) algorithm (Vrugt et al., 2009) rely on multiple parallel chains and utilize a proposal distribution derived from historical chain states to guide sampling toward the target distribution.

The numerical simulation of a single EM forward response becomes more computationally demanding as the spatial dimensions of the problem increase (e.g., from 1 to 2 or 3D). Moreover, the number of parameters required to represent complex geological structures grows exponentially with spatial dimensionality, making the associated inference problem increasingly challenging (Blatter et al., 2021). In this context, a higher number of parameters makes the exploration of the parameter space considerably more demanding for any probabilistic inversion method, thereby increasing the number of forward model evaluations required to reach convergence. Consequently, it is essential to reduce the computational cost of the forward model to ensure that 3D probabilistic inversion remains feasible within reasonable

time frames. Approximate surrogate models are commonly proposed to reduce computational cost, typically offering improved performance in terms of execution time at the expense of reduced accuracy in the EM response. Examples include data-driven surrogates built from regressions between the inputs and outputs of high-fidelity models (e.g. principal component analysis (Köpke et al., 2019), neural networks (Puzyrev, 2019), kriging (Fuhg, 2019), and radial basis functions (Li et al., 2023)). Another category comprises reduced-order models, which project the forward model onto a low-dimensional subspace (e.g. reduced basis methods (Manassero et al., 2020), proper orthogonal decomposition (Allabou et al., 2024), or proper generalized decomposition (Signorini et al., 2017)). Additionally, hierarchical models are constructed from high-fidelity models through simplified physical assumptions, multi-grid strategies, or relaxed convergence tolerances (e.g. Singh & Dehiya, 2025), generally yielding less accurate but computationally cheaper approximations.

The use of surrogate models introduces errors in the forward response, commonly referred to as "modeling error" (Hansen et al., 2014) or "theoretical error" (Tarantola & Valette, 1982) in the context of probabilistic inversion. If not properly accounted for, these errors can lead to biased and overconfident parameter estimates (Köpke et al., 2019). Surrogate models are a compelling alternative for reducing the computational cost of the forward model, provided that the associated modeling errors are adequately addressed (Levy et al., 2021). Several strategies have been developed to handle modeling errors. A common approach is to build statistical models that characterize the discrepancy between a high-fidelity forward model and the surrogate used. For instance, Köpke et al. (2018, 2019) project the data residuals onto orthonormal bases representing the modeling error, constructed either prior to or during the inversion. This allows for the error to be isolated and removed before evaluating the likelihood. Alternatively, Levy et al. (2021) propose a joint inversion of the subsurface model and the modeling error, both parameterized using deep generative neural networks trained for the specific problem at hand. Another strategy, proposed by Manassero et al. (2020), consists in estimating the relative error of the surrogate model at each iteration. If the error exceeds a predefined tolerance, the high-fidelity solution is computed instead, which is then used to enrich the reduced basis of the surrogate model, thereby improving its accuracy in subsequent steps.

Currently, Deep Learning (DL) has emerged as a central topic within modern machine learning and is one of the most active areas of research and application (Dramsch, 2020). Its growing popularity in scientific domains stems from its

versatility, ease of integration into existing workflows, and its effectiveness in processing and extracting insights from large datasets. In the context of EM geophysical methods, DL techniques have been adopted for a range of tasks, including data processing (e.g. Zhang et al., 2022; Luo et al., 2024; Yu et al., 2024), as well as for one-dimensional (e.g. Liu et al., 2022; Wu et al., 2022; Li et al., 2024), 2D (e.g. Pan et al., 2023), and 3D (e.g. Liu et al., 2024) inversion. Given their statistical nature and capacity to handle non-linear problems, machine learning methods are particularly promising for addressing modeling errors. For instance, Xiao (2019) use Gaussian process regression to estimate the residual between a high-fidelity model and a reduced-order model. Their results demonstrate improved agreement between models, even when applied to previously unseen parameters, due to the inclusion of residual error estimation. A similar strategy is employed in Allabou et al. (2024), where neural networks are used not only to approximate the reduced-order forward model, but also to explicitly model the residual error, thereby yielding an accurate and computationally efficient surrogate. In a related study, Corseri et al. (2024) address discrepancies between one-dimensional and 3D model dimensionalities in a one-dimensional Bayesian inversion framework using a machine learning-based correction. A pre-trained model is employed during inversion to estimate the dimensionality compensation error in the magnetotelluric response. A particularly innovative application of DL to geophysical data is addressed by Levy et al. (2021), where deep generative models are used to jointly parameterize the subsurface model and modeling error. Specifically, spatial generative adversarial networks (Jetchev et al., 2017) are trained to learn a nonlinear mapping from high-dimensional data space to a compact "latent" space. This approach enables an efficient 2D probabilistic inversion by jointly inferring the posterior distributions of the latent parameters representing both the subsurface properties and the associated modeling error.

In this work, we employ a combination of methodological strategies to address the computational demands of 3D probabilistic CSEM inversion. First, we design a problem-specific parameterization of the subsurface tailored to the detection and characterization of an offshore hydrocarbon reservoir. To efficiently compute the CSEM response for multiple sources in parallel, we employ a non-conforming finite element iterative solver (Elías et al., 2021). We also introduce a mesh coarsening approach for the discretized conductivity model based on multi-phase Hashin-Shtrikman averaging (Berryman, 1995), enabling a distinction between an accurate forward computation (finely discretized and computationally expensive) and a coarser, more efficient approximate forward computation. Adapting the strategy

introduced by Levy et al. (2021), we incorporate generative neural networks into the inversion scheme to estimate the modeling errors introduced by the use of the approximate forward computation. This set of techniques, combined with a parallel computing in a distributed memory structure over a multi-chain MCMC sampler, enables us to obtain a solution within practical time constraints. We first assess the performance of our methodology using synthetic CSEM data. We then extend its application to field data from a marine CSEM survey.

2 | METHODOLOGY

2.1 | Controlled-source electromagnetic data

CSEM data are used in geophysical research and exploration to characterize the subsurface electrical conductivity distribution. This physical property can be linked to various characteristics of interest, such as reservoir porosity, pore filling, fluid connectivity through fractures, and temperature and salinity in hydrothermal reservoirs (e.g. Manassero et al., 2020; Tveit et al., 2020). Data acquisition involves deploying a controlled EM source near the surface and recording the resulting EM fields with receivers placed around the study area. This approach enhances the signal-to-noise ratio of the measurements, particularly by optimizing source parameters such as dipole moment and signal frequency (Constable, 2006; Ishizu et al., 2024). Furthermore, CSEM methods are non-invasive and cost-effective, capable of providing dense, high-quality datasets at relatively large scales for investigating the Earth's crust.

In particular, frequency-domain marine CSEM is a widely used technique for the exploration and characterization of gas, oil, and CO_2 reservoirs (e.g. Constable, 2006; Christensen & Dodds, 2007; Streich et al., 2013; Tveit et al., 2020; Thorkildsen & Gelius, 2023). This is largely due to its low susceptibility to ambient EM noise and its high sensitivity for mapping strongly resistive layers at depths ranging from several hundred meters to a few kilometers.

2.2 | Three-dimensional forward modeling

Numerical forward modeling is essential for interpreting the behavior of the CSEM response under specific scenarios, particularly considering the regional distribution of electrical conductivity and the configuration of the acquisition system. Accurate numerical solvers are required to simulate the CSEM response of candidate subsurface models within an inversion framework. In the low-frequency regime, Maxwell's diffusive equations are typically solved using algorithms based on four principal numerical approaches: finite differences (FD), integral equation (IE), finite elements (FE), and finite volumes (FV). IE methods offer high computational efficiency for relatively simple conductivity models, however, as model complexity increases, FD, FE, and FV methods are generally preferred due to their flexibility in handling heterogeneous structures. These latter methods rely on 2D or 3D spatial discretizations employing structured or semi-unstructured grids in the case of FD, and structured or fully unstructured grids in FE and FV. A further characteristic of FD, FE, and FV methods is their reliance on the solution of large, sparse systems of equations, which are addressed using either iterative or direct solvers.

In a previous study (Elías et al., 2021), we introduced both an iterative domain decomposition solver and a direct solver for the 3D CSEM forward problem, employing non-conforming FE on non-uniform structured grids. The study demonstrated the high accuracy of the EM responses obtained by both solvers and provided a detailed analysis of their computational performance. While the direct solver exhibited certain advantages, particularly its robustness and efficiency largely invariant to frequency and conductivity structure, the iterative solver showed significantly superior performance in terms of memory consumption and computation time. Therefore, the latter is implemented as the principal forward computing strategy in this work. This choice is further motivated by the iterative solver's inherent suitability for parallelization, owing to its domain decomposition formulation at the differential level. Additionally, the implementation employs a primary-secondary field formulation that enables an accurate semi-analytical representation of the controlled-source field. The application of first-order absorbing boundary conditions (Sheen, 1997) further enhances computational efficiency by reducing the extent of the 3D simulation domain, thereby eliminating the need for padding elements commonly used around the region of interest.

2.3 | Parameterization of the inverse problem

Solving the inverse problem of CSEM data in a probabilistic or Bayesian approach means finding the probability distribution of models that can explain the collected data, given a certain prior distribution. Given a simulator $\mathcal{F}(\cdot)$, the observational data can be modeled as

$$\mathbf{d} = \mathcal{F}(\mathbf{m}) + \boldsymbol{\epsilon}, \tag{2.1}$$

where $\mathbf{d} = \{d_1, \ldots, d_N\}$ denotes the vector of N discrete observations, $\mathbf{m} = \{m_1, \ldots, m_M\}$ represents the vector of M model parameters, and $\boldsymbol{\epsilon}$ accounts for measurement errors and potential simulator-related errors. Then, the posterior probability distribution of the model parameters, conditioned on the observed data, is given by Bayes' theorem (Tarantola & Valette, 1982):

$$\mathrm{p}(\mathbf{m}|\mathbf{d}) = \frac{\mathrm{p}(\mathbf{m})\,\mathrm{p}(\mathbf{d}|\mathbf{m})}{\mathrm{p}(\mathbf{d})}, \tag{2.2}$$

where $\mathrm{p}(\mathbf{d}|\mathbf{m})$ is the likelihood function $\mathrm{L}(\mathbf{m}|\mathbf{d})$, which quantifies the probability of observing the data $\mathbf{d}$ given the model parameters $\mathbf{m}$, $\mathrm{p}(\mathbf{m})$ is the prior probability distribution encoding prior knowledge about the model parameters, and $\mathrm{p}(\mathbf{d})$ denotes evidence, acting as a normalization constant.

Due to the non-linear relationship between the electrical conductivity and the measured EM field, and the complex variations of electrical conductivity in the subsurface, a numerical approach is necessary to sample the posterior pdf. Many possibilities arise in terms of algorithms specifically designed to converge to the posterior pdf efficiently, as we detail in the dedicated section. Regardless of the chosen posterior sampling algorithm, all these procedures rely on performing hundreds of thousands of forward computations (Manassero et al., 2020). This is especially true for complex 3D models and large amounts of model parameters to be inferred. Thus, the achievement of optimal com-

putation time, accuracy and resolution when inverting CSEM data largely relies on (1) the parameterization of the sought model, (2) the discretization of the subsurface electrical conductivity distribution, and (3) the efficiency of the forward response computation.

In this study, we propose to address the parameterization of the inverse problem in a manner specifically tailored to our problem of interest. We adopt a parametric approach to model the 3D distribution of electrical conductivity in a marine subsurface scenario, with the aim of investigating the presence of an oil reservoir. The proposed model focuses on defining a compact set of physical parameters that characterize a potential oil reservoir embedded within a background environment composed of three horizontal layers: air, seawater, and homogeneous sediments. The reservoir is represented as an ellipsoidal body defined by the following parameter set $\mathbf{s} = [\boldsymbol{\alpha}, \boldsymbol{\beta}, \sigma_r, \lambda]$, where $\boldsymbol{\alpha} = (\alpha_1, \alpha_2, \alpha_3)$ defines the semi-axes of the ellipsoid along the x-, y-, and z-direction, respectively, $\boldsymbol{\beta} = (\beta_1, \beta_2, \beta_3)$ specifies the coordinates of the ellipsoid's centroid, σ_r is the conductivity of the reservoir (in S/m), and λ is the conductivity of the surrounding sediment layer. All coordinates are expressed in kilometers, and the z-axis is defined such that $z = 0$ corresponds to the air–seawater interface, with increasing depth in the negative direction. The reservoir is confined within a predefined *exploration zone*, delimited by a rectangular volume with bounds $[x_{ie}, x_{fe}]$, $[y_{ie}, y_{fe}]$, and $[z_{ie}, z_{fe}]$. The reservoir parameterization only applies within this region, in cases where the ellipsoid extends beyond these boundaries, it is effectively truncated.

Once the subsurface parameters are established, they are embedded into a non-uniform structured 3D finite element grid, which exhibits a higher element density over the exploration zone in the horizontal plane (x and y), and a refined vertical resolution (z) centered around the depth of the reservoir centroid. This mesh design ensures an adequate resolution for both the anomaly and the surrounding medium. The conductivity values are assigned to each element in the grid as follows. Outside the exploration zone, the conductivity corresponds to that of the background medium (air, seawater, or sediment). Inside the exploration zone, for each element centered at coordinates (x, y, z), the conductivity is set to σ_r if the point lies within the ellipsoid defined by the inequality

$$\frac{(x-\beta_1)^2}{\alpha_1^2} + \frac{(y-\beta_2)^2}{\alpha_2^2} + \frac{(z-\beta_3)^2}{\alpha_3^2} \leq 1, \tag{2.3}$$

and to λ otherwise. This base model comprises the regional conductivity distribution and the appropriately refined discretization required for solving the forward problem. Therefore, the parameter vector $\mathbf{s}$ serves as a useful representation of an anomalous body within the study region.

Computing the EM response on a refined FE grid is highly demanding, even when employing our efficient non-conforming FE iterative solver (Elías et al., 2021). To address this limitation, we propose a surrogate modeling methodology that generates a secondary FE grid with a reduced number of elements and a coarser discretization of the conductivity distribution. This approach enables a more efficient computation of the EM response, at the expense of a moderate loss of accuracy. Let the original fine grid be composed of $n_x^{\mathrm{f}} \times n_y^{\mathrm{f}} \times n_z^{\mathrm{f}}$ elements, where n_x^{f}, n_y^{f}, and n_z^{f} denote the number of elements along the x-,y-, and z-direction, respectively. The coarsened grid covers the same 3D domain but with $n_x^{\mathrm{c}} \times n_y^{\mathrm{c}} \times n_z^{\mathrm{c}}$ elements, where $n_x^{\mathrm{f}} > n_x^{\mathrm{c}}$, $n_y^{\mathrm{f}} > n_y^{\mathrm{c}}$, and $n_z^{\mathrm{f}} > n_z^{\mathrm{c}}$. The coarsening procedure consists of the following steps:

1. Superimpose both grids within the same 3D domain.
2. For each coarse voxel, identify the q fine voxels whose volume overlaps, at least partially, with that of the coarse voxel.
3. Determine the q fractional overlaps and their associated conductivity values from the fine-scale model.
4. Identify unique conductivity values among the q fine voxels. Let r denote the number of unique conductivities. Compute the corresponding r aggregated fractions by summing the fractional volumes associated with repeated conductivity values.
5. Assign to the coarse voxel an averaged conductivity value given by a function $\mathrm{C}(\hat{\boldsymbol{\sigma}}, \hat{\boldsymbol{\theta}})$, where $\hat{\sigma}$ and $\hat{\boldsymbol{\theta}}$ are the vectors of the r unique conductivities and their respective volume fractions.

The latter averaging process relies on the multi-phase Hashin-Shtrikman bounds approach (Berryman, 1995), ensuring the preservation of relevant conductivity distribution of the original model. It enables the assignment of a conductivity value that better represents the phase composition compared to a simple weighted average, although it does not preserve information on the contact orientation between the phases. A detailed procedure description is provided in

Appendix 5.

The outcome of this process is an approximate conductivity distribution defined over the coarse FE grid. This approximate model can be used to compute an approximate EM forward response, enabling a surrogate, faster inversion, while accepting the trade-off of reduced solution fidelity. In brief, given a parametric model $\mathbf{s}$ we are proposing its discrete representation on a refined (accurate) FE grid, along with a coarse (approximate) FE grid. This allows us to compute the simulated EM response using both an accurate forward computation, $\mathrm{f}^{\mathrm{acc}}(\mathbf{s})$, which is computationally expensive, and an approximate forward computation, $\mathrm{f}^{\mathrm{app}}(\mathbf{s})$, which is more efficient.

Therefore, given a set of observations from a CSEM experiment, the data vector $\mathbf{d}$ is theoretically related to the parametric model $\mathbf{s}$ through the following equation

$$\mathbf{d} = \mathrm{f}^{\mathrm{acc}}(\mathbf{s}) + \boldsymbol{\epsilon}, \tag{2.4}$$

where $\boldsymbol{\epsilon}$ is a vector that accounts for both data measurement errors and discrepancies arising from model parameterization or intrinsic deficiencies in the forward $\mathrm{f}^{\mathrm{acc}}$ solution. Alternatively, we can use the approximate forward computation $\mathrm{f}^{\mathrm{app}}$ in the aforementioned relation, such that

$$\mathbf{d} = \mathrm{f}^{\mathrm{app}}(\mathbf{s}) + \boldsymbol{\xi} + \boldsymbol{\epsilon}, \tag{2.5}$$

where $\boldsymbol{\xi}$ represents a correction term to account for the discrepancy between the approximate and accurate forward EM responses. Our strategy involves incorporating the relationship expressed in equation (2.5) into the inversion process, thereby leveraging the computational efficiency provided by the approximate forward computation. However, this necessitates providing an explicit expression for the correction term $\boldsymbol{\xi}$, as it is not negligible, and ignoring it could introduce biases into the simulation (Hansen et al., 2014; Levy et al., 2021). We propose to develop a statistical model

for the correction $\boldsymbol{\xi}$ using DL techniques. This approach incorporates a prior distribution of the $\mathbf{s}$ model parameters and generates a set of $\boldsymbol{\xi}$ samples for training, based on the expression

$$\boldsymbol{\xi}(\mathbf{s}) = \mathsf{f}^{\mathrm{acc}}(\mathbf{s}) - \mathsf{f}^{\mathrm{app}}(\mathbf{s}). \tag{2.6}$$

2.4 | Deep-learning-assisted modeling error

In this section, we describe the DL techniques employed and their use for constructing the statistical model of the $\boldsymbol{\xi}$ correction discussed earlier.

DL networks, also referred to as feedforward networks, can be conceptualized as function approximation mechanisms designed to achieve statistical generalization (Goodfellow et al., 2016). In particular, Convolutional Neural Networks, have constituted a breakthrough in the development of adaptive systems (Puzyrev, 2019), such as image classification and time-series processing (He et al., 2016; Wibawa et al., 2022). Their impact on computer engineering is due to their straightforward mathematical formulation, which involves applying convolution filters, feature maps, or kernels within a layered structure that combines both efficiency and versatility. The convolution operation is computationally cost-effective when using short filters, and the capability to represent increasingly complex systems is attained by incorporating a greater number of layers (depth) into the network (Dramsch, 2020; Yu & Ma, 2021).

DL networks enable the construction of a representative function from a dataset (training data) through an adaptive process known as training. During this process, the network performs feature mapping of the dataset by determining or adjusting (learning) the parameters (weights) that constitute the network. The manner in which a network interacts with the data during training varies depending on its intended purpose. In particular, deep generative models represent probability distributions over multiple variables (Goodfellow et al., 2016), which motivates our interest to use them in the construction of a statistical model of the modeling error.

In this work, we use Generative Adversarial Networks (GANs), a specialized type of Convolutional Neural Network (Creswell et al., 2018). In GANs, the adaptive process is structured as a zero-sum theoretic game (Goodfellow et al.,

2016), where a generator network G competes against an adversarial discriminator network D. In particular, we employ the spatial extension of GANs (spatial-GAN, Jetchev et al. (2017)), in which the input noise space distribution is reformulated from a single vector $\mathbf{z}$ to a 2D spatial tensor $\mathbf{z}$, randomly drawn from a prior distribution $p(\mathbf{z})$ (e.g., Gaussian, uniform). The generator G produces a 2D, multi-channel output array, denoted as $\hat{\boldsymbol{\xi}}$, in direct analogy with the correction term $\boldsymbol{\xi}$ expressed in equation (2.6). The discriminator D receives input samples $\boldsymbol{\xi}$ from the training set or samples $\hat{\boldsymbol{\xi}}$ generated by the network G. Thus, $D(\boldsymbol{\xi})$ or $D(\hat{\boldsymbol{\xi}})$ should produce a scalar value indicating the probability that the input data is a true sample $\boldsymbol{\xi}$ rather than a "fake" sample $\hat{\boldsymbol{\xi}}$. The concept of a zero-sum game in this context means that the successful performance of G (the generator) corresponds to a similar failure by D (the discriminator), and vice versa. During the adaptive process, both networks aim to maximize their performance. A key characteristic of GANs is that the adaptive process aims to minimize the distance between two distributions. During training, the weights of the generator network G are adjusted so that the distribution $p_G(\hat{\boldsymbol{\xi}})$ of the generated data increasingly approximates the distribution $p_{data}(\boldsymbol{\xi})$ of the training set. In Arjovsky et al. (2017), various methods for measuring the distance between distributions are compared, demonstrating the advantages of the Wasserstein-1 distance in enhancing the stability of GAN learning. Consequently, in this paper, we address the following simultaneous optimization problem to adapt the parameters of the D and G networks, based on the Wasserstein-GAN algorithm:

$$\min_{G} \max_{D \in \mathcal{D}} \quad \mathbb{E}_{\boldsymbol{\xi} \sim p_{data}}[D(\boldsymbol{\xi})] - \mathbb{E}_{\mathbf{z} \sim p_G}[D(G(\mathbf{z}))]. \tag{2.7}$$

In the context of Wasserstein-GANs, the D network is referred to as "critic" because its output is not interpreted as a probability but rather as a score for estimating the distance between distributions.

Regarding the GAN architecture used in this work (summarized in Table 1), we rely on the framework outlined by Levy et al. (2021). The network is purely convolutional, with the generator input $\mathbf{z}$ being a 2D array, which facilitates a tight spatial relationship between perturbations in one element of the input array and their effects on regions of the output (Jetchev et al., 2017). Both G and D networks consist of four sequentially stacked layers but differ in the operations performed internally. For the generator network G, transposed convolution operations increase the

spatial dimensions of the output at each layer. Conversely, the critic network D uses convolution operations that reduce the spatial dimensions. In both cases, the dimensionality of the final output is controlled by the input layer dimensions, the number of layers, the stride and padding parameters. Stride and padding hyperparameters control how convolution filters move across the input in each layer: stride determines the step size for filter movement, affecting the spatial dimensions of the output, while padding adds extra pixels around the input to preserve or alter the output size. Additionally, the size of the convolution filters is 5×5 for both networks, but the number of filters increases as the spatial dimensions are reduced. In each successive layer, except for the final one, the generator applies the Parametric Rectified Linear Unit (PReLU) activation function (He et al., 2015), followed by instance normalization (Ulyanov et al., 2017), which normalizes the feature maps across their spatial dimensions for each instance. In the final layer, however, the generator applies only a hyperbolic tangent as activation function, scaling the output to a range between -1 and 1. Therefore, the training data must be normalized within this range to ensure comparability with the generated data. Regarding the critic D, after the convolution operation in each layer, the filter weights are normalized by applying spectral normalization, which ensures the preservation of the Lipschitz continuity condition required in the context of Wasserstein-GANs. Following this, Mean Spectral Normalization is applied to the first three layers, which, according to Subramanian & Chong (2019), is a necessary reparameterization that significantly improves network performance. Finally, all layers except for the last one apply a Leaky Rectified Linear Unit (LeakyReLU) activation function (Maas et al., 2013).

In Section 3, we provide the implementation details of this generative model, aimed at constructing a parameterized statistical representation of the discrepancies between forward models. This representation is then employed as a correction to the approximate forward computation within the inversion process.

2.5 | Inversion via Bayesian inference

In the framework of Bayesian inference, our probabilistic inversion problem aims to estimate the posterior pdf conditioned on the observed data. Given equation (2.5), which theoretically relates the observed data $\mathbf{d}$ to the parameters of the physical model $\mathbf{s}$, we introduce the parameters $\mathbf{z}$ in order to estimate a correction $\hat{\boldsymbol{\xi}} = \mathrm{G}(\mathbf{z})$ to the approximate

forward computation using a trained generative network. That is

$$\mathbf{d} = \mathrm{f}^{\mathrm{app}}(\mathbf{s}) + \kappa \mathrm{G}(\mathbf{z}) + \epsilon, \tag{2.8}$$

where an additional scaling parameter, κ, is introduced to modulate the correction term. This parameter serves to regulate the magnitude of the applied correction, with the objective of enhancing its effectiveness and stability during the inference process (Levy et al., 2021).

Let the set of parameters under investigation be defined as a vector of dimension M, $\mathbf{m} = [\mathbf{s}, \mathbf{z}, \kappa] = (m_1, \ldots, m_M)$, and the set of observed data be organized in a vector of dimension N, $\mathbf{d} = (d_1, \ldots, d_N)$. These can be related through Bayes' theorem (Tarantola & Valette, 1982) by means of the posterior pdf introduced in equation (2.2). In this expression the evidence $\mathrm{p}(\mathbf{d})$ is a normalization constant that, in cases of a fixed model parameterization, can be omitted, leading to the unnormalized proportionality or posterior equality $\mathrm{p}(\mathbf{m}|\mathbf{d}) \propto \mathrm{p}(\mathbf{m})\mathrm{L}(\mathbf{m}|\mathbf{d})$, where, as mentioned earlier, $\mathrm{L}(\mathbf{m}|\mathbf{d})$ denotes the likelihood function. The prior probability of the parameters $\mathbf{m}$ encapsulates information both about the subsurface before the data is collected and about the behavior of the error associated with the approximate forward computation.

The likelihood represents a measure of the discrepancy between the observed data and the simulated model. The closer the two are, the higher the value of the function. It is common to assume that measurement errors are uncorrelated and follow a zero-mean normal distribution. Consequently, we can express the log-likelihood, which is the logarithm of the likelihood function, as follows:

$$\mathrm{l}(\mathbf{m}|\mathbf{d}) = -\frac{N}{2}\log(2\pi) - \frac{1}{2}\log\left(\prod_{i=1}^{N}\sigma_i^2\right) - \frac{1}{2}\sum_{i=1}^{N}\left(\frac{d_i^{\mathrm{sim}} - d_i}{\sigma_i}\right)^2, \tag{2.9}$$

where σ_i represents the standard deviation of the i-th measurement error ϵ_i, and d_i^{sim} is the i-th simulated data point with equation (2.8). The summation in the third term of this equation represents the data misfit, which quantifies the distance between the simulated data and the observed data. As this distance decreases, an increase in the log-likelihood indicates a higher probability that the proposed parameters belong to the posterior pdf. Given the assumptions about measurement errors, the data misfit follows a χ^2 distribution with an expected value of N. Consequently, the expression for the root mean square (RMS) misfit is

$$\text{RMS} = \sqrt{\frac{1}{N}\sum_{i=1}^{N}\left(\frac{d_i^{\text{sim}} - d_i}{\sigma_i}\right)^2}, \tag{2.10}$$

which is practical due to its expected value of one and its independence from the number of measurements.

In scenarios like ours, where the inversion problem is high-dimensional and nonlinear, it is not feasible to evaluate the posterior pdf analytically, therefore, numerical sampling methods are employed to approximate it (Tarantola, 2005). One of the most popular and widely utilized methods is the MCMC method, which iteratively explores the parameter space through a guided random walk. This process begins by proposing a starting point $\mathbf{m}_{\text{old}}$ sampled from the prior distribution. In subsequent iterations, new points are proposed, which must be accepted to form part of the posterior pdf. A new candidate point $\mathbf{m}_{\text{new}}$ is generated from a proposal distribution that is conditioned on the last accepted point. The proposal $\mathbf{m}_{\text{new}}$ is then accepted or rejected based on an acceptance probability, which, in the case of a uniform prior, is given by (Mosegaard & Tarantola, 1995)

$$\text{P}_{\text{accept}} = \min\{1, \exp[\,\text{l}(\mathbf{m}_{\text{new}}|\mathbf{d}) - \text{l}(\mathbf{m}_{\text{old}}|\mathbf{d})\,]\}. \tag{2.11}$$

At each step, if the proposal is accepted, the Markov chain advances, and $\mathbf{m}_{\text{new}}$ becomes $\mathbf{m}_{\text{old}}$, otherwise, the chain remains unchanged. The acceptance probability guides the chain, ensuring that after a sufficient number of iterations,

its elements are distributed according to the posterior distribution. The selection of the proposal distribution for new candidates, along with its scale and orientation, is a critical factor in achieving efficient sampling and enhancing the convergence rate. This efficiency can be quantified by the acceptance rate of new candidates, if this rate is too low, it indicates that the chain does not progress between iterations, which may result from an inappropriate choice of distribution. Thus, a judicious selection of the proposal distribution facilitates the swift advancement of the chain between iterations, thereby accelerating convergence.

In this work, we employ the DiffeRential Evolution Adaptive Metropolis ($\text{DREAM}_{(\text{ZS})}$) (Laloy & Vrugt, 2012) sampling algorithm. It is specifically designed to address non-linear and high-dimensional problems by effectively exploring the posterior distribution. Additional features of the algorithm, such as adaptive randomized subspace sampling, multi-chain pairs for generating new candidates, mixing between parallel direction and snooker jumps, and outlier detection, enhance the speed of convergence of the chains to the limiting distribution, which corresponds to the posterior distribution. Multiple independent Markov chains are run in parallel, and differential evolution (Price et al., 2005) is used to propose jumps based on samples drawn from an archive of past states of the joint chains. Utilizing past states reduces the number of chains required to effectively explore the target distribution and facilitates the application of the algorithm in high-dimensional spaces (Vrugt, 2015). Moreover, relying solely on historical states enhances the parallel implementation by improving the evolution of different trajectories. A key parameter in the proposal mechanism is the jump rate, defined as $\gamma = 2.38\upsilon_0/\sqrt{2\delta Q^*}$, where υ_0 is a scaling factor, δ is the number of candidate pairs used to construct the jump, and Q^* is the number of dimensions modified according to a crossover probability (Vrugt, 2015). In addition, a probability of 20% is assigned to setting $\gamma = 1$ ($\text{p}(\gamma = 1) = 0.2$) to enable jumps between disconnected modes of the target distribution (ter Braak & Vrugt, 2008). This adaptive strategy, which automatically adjusts the proposal distribution, addresses a practical limitation of random walk methods, particularly the random walk Metropolis algorithm, by appropriately tuning the scale and orientation of the jump distribution. Moreover, the periodic calculation of the Gelman-Rubin statistic (Gelman et al., 1992) is used to assess convergence to the posterior distribution. The following criterion is applied: convergence is established when the analysis of the final 50% of the chains yields Gelman-Rubin statistics less than 1.2 for all parameters.

Using $\text{DREAM}_{(\text{ZS})}$, we infer the posterior distribution of the parameter space $\mathbf{m} = [\mathbf{s}, \mathbf{z}, \kappa]$. This includes the param-

eters of the physical subsurface model $\mathbf{s} = [\alpha, \beta, \sigma_r, \lambda]$, i.e., the shape ($\alpha$), position ($\beta$), reservoir conductivity (σ_r), and the conductivity of the surrounding sediments (λ). We choose uniform prior distributions, $\mathcal{U}(u_{\min}, u_{\max})$, for these variables, with the bounds defined individually for each parameter. In addition, $\mathbf{m}$ includes the latent space $\mathbf{z}$, which is the parameterization of the forward model correction and we also choose the least-informative uniform prior distribution $\mathcal{U}(-1, 1)$, and the correction scaling factor κ, which is assigned a uniform prior distribution $\mathcal{U}(0, \kappa_{\max})$.

Algorithm 1 Inversion with Deep-learning-based, surrogate model correction using DREAM$_{(ZS)}$

Create the archive with realizations $\mathbf{m} = [\mathbf{s}, \mathbf{z}, \kappa]$ randomly from prior distributions $p(\mathbf{s})$, $p(\mathbf{z})$, and $p(\kappa)$.
For each Markov chain, with $t = 0$ initialize the starting point $\mathbf{m}^t_{\text{old}} = [\mathbf{s}^t, \mathbf{z}^t, \kappa^t]$.
$\mathbf{d}^{\text{sim}} = f^{\text{app}}(\mathbf{s}^t) + \kappa^t \hat{\boldsymbol{\xi}}^t$, where $\hat{\boldsymbol{\xi}}^t = G(\mathbf{z}^t)$.
Compute the likelihood $l(\mathbf{m}^t_{\text{old}}|\mathbf{d})$ (equation (2.9)), where $\mathbf{d}$ is the observed data.
Set $t = 1$.
while $t < N_{\text{draw}}$ **do**
    Generate a random realization $\mathbf{m}_{\text{new}} = [\mathbf{s}', \mathbf{z}', \kappa']$ from DREAM$_{(ZS)}$ proposal distribution.
    $\mathbf{d}^{\text{sim}} = f^{\text{app}}(\mathbf{s}') + \kappa' \hat{\boldsymbol{\xi}}'$, where $\hat{\boldsymbol{\xi}}' = G(\mathbf{z}')$.
    Compute the likelihood $l(\mathbf{m}_{\text{new}}|\mathbf{d})$
    Calculate the acceptance probability $a \leftarrow \exp\left(l(\mathbf{m}_{\text{new}}|\mathbf{d}) - l(\mathbf{m}^{t-1}_{\text{old}}|\mathbf{d})\right)$
    Draw A from uniform distribution $\mathcal{U}(0, 1)$
    if $A < a$ **then**
        $\mathbf{m}^t_{\text{old}} = [\mathbf{s}^t, \mathbf{z}^t, \kappa^t] \leftarrow \mathbf{m}_{\text{new}} = [\mathbf{s}', \mathbf{z}', \kappa']$
    else
        $\mathbf{m}^t_{\text{old}} = [\mathbf{s}^t, \mathbf{z}^t, \kappa^t] \leftarrow \mathbf{m}^{t-1}_{\text{old}} = [\mathbf{s}^{t-1}, \mathbf{z}^{t-1}, \kappa^{t-1}]$
    end if
    if t is a multiple of the archive addition rate **then**
        Add $\mathbf{m}^t_{\text{old}}$ to the external archive.
    end if
    $t = t + 1$
end while

| Use of Artificial Intelligence tools in the writing process

The authors declare that, during the writing process, ChatGPT (OpenAI, GPT-5.1, 2025) was used solely to assist with grammar correction and improvements in readability. All outputs provided by the tool were reviewed and edited by the authors to preserve the authenticity and rigor of the original text. The authors assume full responsibility for the final content of the manuscript.

3 | RESULTS

3.1 | Synthetic example of a marine experiment

To evaluate our inversion methodology, we propose a synthetic example that replicates the main features of a marine CSEM experiment. The 3D synthetic conductivity model consists of three flat layers representing a scenario with air, 2.7 km of seawater, and a sediment half-space, with conductivities of 10^{-14}, 3.33, and 0.5 S/m, respectively. Positioned at a depth of approximately 2.57 km below the seafloor, the model incorporates a lenticular, high-resistivity anomaly with an estimated thickness of 200 m and lateral extensions of roughly 4.5 km in the x-direction and 2 km in the y-direction. This body emulates a hydrocarbon reservoir characterized by a reduced electrical conductivity of 10^{-3} S/m, in contrast to the more conductive surrounding sediments (Figure 1). A uniform array of 16×16 seabed receivers was deployed across a central exploration zone, which has a volume of 12 km $\times$12 km $\times$2.3 km with its top located at depth of 3.6 km relative to the sea level. The EM source consists of a horizontal electric dipole (HED), aligned along the x-axis and placed 50 m above the seafloor, with a horizontal offset of 9 km in the x-direction from the center of the receiver grid. The CSEM data comprises the real and imaginary components of the x- and y-oriented electric field at each receiver location, for excitation frequencies of 1.0, 0.5, 0.25, and 0.05 Hz. The synthetic observations were contaminated with noise by assuming Gaussian-distributed measurement errors, with a standard deviation $\sigma_{\mathbf{d}}$ defined relative to the amplitude F of each measurement as follows:

$$\sigma_{\mathbf{d}}/F = \sqrt{b^2 + (a/F)^2}, \tag{3.1}$$

where b is a relative noise level, set to 0.02, and a is the absolute noise level of the measurement set, set to 4×10^{-17} V/A/m^2 (Christensen & Dodds, 2007). A threshold amplitude of 2×10^{-16} V/A/m^2 was set as the minimum detectable level, with synthetic data below this value being discarded.

For the purposes of this study, we restrict the set of unknowns in the synthetic experiment to the reservoir's shape

(α) and location (β). Thus, the conductivity parameters of the sediments (λ) and the reservoir (σ_r) are assumed to be known. Consequently, the vector of subsurface parameters to be inferred through the proposed inversion scheme is given by $\mathbf{s} = [\alpha, \beta]$.

3.1.1 | Generative model implementation

To implement the generative model, a database of 32,000 correction samples $\boldsymbol{\xi}$ was created for training the neural network. This process involved sampling 32,000 realizations from the prior distribution of the reservoir parameterization $\mathbf{s}$ (Table 2) and computing the EM responses using both the accurate (f^{acc}) and approximate (f^{app}) forward models. The computation of the full database required approximately 2.14 d on a node equipped with 128 processors and 30 GB of memory. On average, each approximate forward computation required 3 s, whereas the corresponding accurate forward computation demanded 30 s (Table 3). The correction $\boldsymbol{\xi}$ was then calculated using equation (2.6). Both forward models were constructed based on the characteristics of the previously described synthetic example, with the distinction that the accurate forward computation employed a discretization grid of $80 \times 80 \times 40$ elements, while the approximate forward computation used a coarser grid of $40 \times 40 \times 24$ elements. In this synthetic test case, we chose to focus on inverting only the parameters related to the shape and location of the reservoir, keeping the reservoir conductivity fixed at 10^{-3} S/m and the sediments conductivity at 0.5 S/m.

Once the database was computed, a mask was applied to retain only the data points not discarded by the detectability restriction. Next, the distribution of the dataset was analyzed to assess the magnitude and variability of the modeling errors relative to the assumed measurement error standard deviation $\sigma_{\mathbf{d}}$. For the frequencies 1., 0.5, 0.25, and 0.05 Hz, the percentages of samples in the database with at least one data point exceeding the measurement error standard deviation are 1.6%, 9.3%, 26.8%, and 59.0%, respectively. Figure 2 presents density histograms of the absolute value of $\boldsymbol{\xi}$ from the database, expressed as a percentage of the amplitude (F) of the synthetic observed data, for various frequencies, components, and a subset of receivers along the x direction. When compared to the corresponding percentage measurement error for each component, it is evident that the database includes samples of $\boldsymbol{\xi}$ that significantly exceed the measurement error, indicating that the difference between the accurate and approximate forward

EM responses is not negligible. Considering that at high frequencies the offset where good EM data can be measured is reduced, resulting in less informative data compared to lower frequencies, and noting that at the frequency of 1 Hz only 1.6% of the database contains samples exceeding the measurement error, we opted to exclude this frequency and retain only the remaining three frequencies for training the generative network. Furthermore, we removed from the training database all samples whose amplitude did not exceed the standard deviation $\sigma_{\mathbf{d}}$ of the measurement error at any measurement point.

To train the neural network, we employed a training database comprising 18,890 samples, each with 12 channels of size 16×16. The number of channels corresponds to the combination of 3 frequencies and the real and imaginary parts of the electric field components in the x- and y-direction. To satisfy the input and output requirements of the generator and discriminator, respectively, the database was normalized to the range $(-1, 1)$ by using the global minimum and maximum values per channel across the entire database. During training, the normalized database was used to randomly assemble batches of 64 samples, which were jointly used to update the network weights at each iteration. Although, in general, each update of the generator network corresponds to a single update of the discriminator network (a 1 : 1 ratio), during the first 25 iterations and periodically every 100 iterations, the update ratio is modified to 1 : 100. The generative network was trained for 5,000 epochs, each consisting of 100 iterations, using an A100GPU with 40 GB of memory, with a total training time of 4.32 h.

Once the generative network is trained, we reduced the number of parameters required to represent the correction $\boldsymbol{\xi}$, originally defined in a space of dimension equal to the length of the synthetic data (i.e., 2025 points after considering only 3 frequencies and applying a minimum amplitude mask), to the latent space $\mathbf{z}$, with size $4 \times 4 \times 1$. To assess the fidelity of our statistical model, we computed the pointwise mean and standard deviation of a set of 18,890 fake realizations created by the generator network G and compared them with the corresponding statistics from the training database. Figure 3 presents a comparison of the aforementioned statistical measures between the generator network G outputs and the training database, illustrating 4 out of the 12 components (channels). Both the mean and standard deviation computed from the generative model effectively match the order of magnitude of those derived from the training realizations across all displayed components. Additionally, the spatial distribution of these quantities over the xy receiver grid exhibits coherent patterns between the two sets, although the training set displays smoother varia-

tions, characteristic of its numerical origin. These results indicate that the main statistical properties are well captured by our correction model, which is compact in terms of parameters and provides practically instantaneous evaluation per realization.

3.1.2 | Synthetic data inversion

We carried out the inversion of the synthetic data for frequencies of 0.5, 0.25, and 0.05 Hz. The synthetic data was generated using the accurate forward computation ($\mathrm{f}^{\mathrm{acc}}$), whose FE grid comprises $80 \times 80 \times 40$ elements, as illustrated in Figure 1. As previously described, the data was contaminated with random Gaussian noise and a mask was applied eliminating measurements below a certain detectability level, resulting in a total of 2025 measurement points. During the inversion procedure, we employed the surrogate modeling strategy (Section 2.3, Algorithm 1), where we calculate the forward EM response using a coarser mesh, involving a smaller number of conductivity voxels, and approximate conductivity values for each voxel. Consequently, the EM response is computed on a coarser FE grid consisting of $40 \times 40 \times 24$ elements. We consider the inversion of four distinct scenarios: (1) inversion of the six parameters in $\mathbf{s}$ describing the shape and location of the anomaly, without correcting the approximate forward computation (referred to as '$\mathrm{f}^{\mathrm{app}}$ without correction'); (2) inversion of the six parameters in $\mathbf{s}$, the 16-dimensional array $\mathbf{z}$, and a scaling factor κ modulating the correction $\boldsymbol{\xi}$ (referred to as '$\mathrm{f}^{\mathrm{app}}$ with scaled correction'); (3) inversion of the six parameters in $\mathbf{s}$ using the accurate forward computation $\mathrm{f}^{\mathrm{acc}}$ (referred to as '$\mathrm{f}^{\mathrm{acc}}$'); and (4) a variant of case (2), in which the correction is not applied during the initial 3,000 iterations (referred to as '$\mathrm{f}^{\mathrm{app}}$ with delayed and scaled correction'). The prior distributions for the parameters defining the shape of the anomaly, $\mathbf{s} = [\alpha, \beta]$, are summarized in Table 2. The horizontal coordinates of the anomaly centroid are restricted to discrete values spaced approximately 182 m apart, consistent with the discretization of the spatial domain. The latent variables $\mathbf{z}$ and the scaling parameter κ follow uniform prior distributions $\mathcal{U}(-1, 1)$ and $\mathcal{U}(0, 3)$, respectively.

We employ the $\mathrm{DREAM}_{(\mathrm{ZS})}$ algorithm in combination with the CSEM forward modeling approach based on non-conforming FE domain decomposed iterative solver (Elías et al., 2021), which together enable an optimal parallel computing architecture for efficient MCMC simulation. In particular, we run three parallel chains, each evaluating the

EM response concurrently, while the forward solver further parallelizes computations internally across its dedicated cluster of processors. Additionally, the employed DL libraries offer high parallelization efficiency across the available processor domain, allowing the generative network to contribute to the inversion process with negligible latency. The total number of processors used in the synthetic inversion is 90, distributed evenly among the forward computations for each chain, or dynamically allocated when neural network evaluations are required. Since the runtime of the iterative FE solver varies with frequency (Elías et al., 2021), the EM responses at the three frequencies are computed sequentially. On average, a full iteration takes approximately 1.5 s when using the approximate forward computation (with or without correction), and 9.3 s when using the accurate forward computation.

The inversion using $\mathrm{f}^{\mathrm{app}}$ with scaled correction reaches convergence after 22,890 iterations, requiring a total time of 10.12 h. The alternative case, where the correction is applied after an initial delay, converges slightly faster at 21,190 iterations in 9, 23 h. In contrast, the inversion with $\mathrm{f}^{\mathrm{app}}$ without correction, which involves fewer parameters, achieves convergence in only 9,890 iterations over 4.22 h. Similarly, the case using the accurate forward computation $\mathrm{f}^{\mathrm{acc}}$ converges in 9,910 iterations but requires significantly more computational time, 25.72 h. It is important to highlight that after identifying convergence at a given number of iterations, we continue sampling up to four times that amount of iterations in order to sample the posterior pdf (Laloy & Vrugt, 2012). Table 4 summarizes the total runtime of each inversion. The use of the approximate forward computation with correction demands approximately one third of the computational time required by the inversion with an accurate forward computation. Additionally, the data misfit is improved in cases where the correction is incorporated into the approximate forward computation. Figure 4 and Table 2 present a comparative analysis of the posterior pdfs and associated statistical metrics for the four inversion strategies. The marginal posterior distributions are shown for each of the reservoir parameters, the extensions along the x-, y-, and z-axes, as well as the spatial coordinates of the reservoir centroid. The true values from the synthetic model are also indicated for reference. Overall, the incorporation of the correction into the approximate forward computation effectively reduces bias in the inferred posterior distributions. In particular, the marginal distributions for the reservoir dimensions exhibit increased probability density around the true values, confirming that the correction enhances the reliability of the inversion results. In particular, the strategy involving a delayed application of the correction appears to yield posterior distributions concentrated around the true values of the reservoir parameters. This behavior can be

attributed to the benefit of initially exploring the parameter space associated with the subsurface structure, allowing the generative correction to subsequently focus on addressing the specific limitations of the approximate forward computation in reproducing the EM data. Regarding the reservoir location, all inversions, disregarding of whether the correction is applied, result in posterior distributions reasonably close to the true centroid position. However, limitations in horizontal resolution are clear, likely due to the coarse discretization employed, which constrains the model's ability to resolve fine-scale spatial variability.

3.2 | Data field example of a marine experiment

We applied our methodology to real marine CSEM data acquired the southern Campos Basin, Brazil, approximately 315 km from Río de Janeiro, as part of an exploration project aimed at characterizing potential hydrocarbon reservoirs. The dataset consists of measurements collected along two receiver lines, denoted L1 and L2, and includes electric field amplitude and phase components aligned with the direction of each acquisition line. The source used was a HED positioned approximately 50 m above the flat seabed, oriented along each acquisition line in both cases. Line L1 comprises 24 receivers deployed at roughly 1 km intervals over a total length of 25 km, with a SW–NE orientation (Figure 5a). We selected three source positions along L1, spaced every 6 km, transmitting at frequencies of 0.25 and 0.75 Hz. Line L2 consists of 22 receivers spaced similarly over 21 km in a NW–SE orientation. We selected for this line two source positions spaced 7 km apart, operating at frequencies of 0.5 and 1.5 Hz. The two acquisition lines intersect at an angle of approximately 52 degrees. The arrangement of the lines is shown schematically in Figure 5a. The acquiring company provided the absolute noise levels in amplitude (a) of the survey. These are 7×10^{-16}, 3×10^{-16}, 8×10^{-16}, and 5×10^{-16} V/A/m^2 for the frequencies 0.25, 0.5, 0.75, and 1.5 Hz, respectively (Table 5). Assuming a relative noise level (b) of 0.02 for each amplitude measurement (F), the uncertainty in the electric field amplitude, denoted as $\sigma_{\mathbf{d}}^{\mathrm{a}}$, was computed using equation (3.1). In addition, the uncertainty in the electric field phase ($\sigma_{\mathbf{d}}^{\mathrm{p}}$) was determined

following the formulation proposed by Christensen & Dodds (2007), as follows:

$$\sigma_{\mathbf{d}}^{\mathrm{p}} = \sqrt{b_{\mathrm{p}}^2 + c^2}, \tag{3.2}$$

where b_{p} is a minimum uncertainty bound in the determination of phase, which we set at 0.035 radians (2 degrees), and c is an absolute noise level assigned to each group of sources and receivers. Following the criterion established by Christensen & Dodds (2007), we assume that the quality of phase measurements decreases with increasing source-receiver offset, reaching a maximum uncertainty at a distance R (Table 5), beyond which the phase becomes undetectable. According to this model, c remains zero for offsets less than $R/2$, and increases smoothly from zero to 0.5 radians in the interval between $R/2$ and R. Once all data points for each receiver, source, frequency, and component have been collected, the data vector $\mathbf{d}$ consists of 204 elements.

To parameterize the subsurface conductivity we chose a system of six horizontal layers (Figure 5), where the first layer corresponds to an air half-space and the second layer, with a thickness of 2.7 km, represents seawater. These layers have fixed conductivities of 1×10^{-14} and 3.33 S/m, respectively. Based on a seismic section acquired along line L1, four subsurface layers were interpreted. These layers have topography that follow the interpreted horizons of the seismic section (Figure 5b). The conductivity of each layer was assumed to be laterally homogeneous and treated as a parameter to be estimated during inversion, except for the penultimate layer, whose conductivity was fixed at 1×10^{-3} S/m, assuming that it consists predominantly of halite. Given the lithological characteristics of the different strata obtained from a borehole drilled in the region, and the interpreted seismic section, the reservoir rock is assumed to be located within the second subsurface layer, with the overlying layer acting as a seal. The hydrocarbon reservoir was parameterized as an ellipsoidal lens entirely contained within the second layer. Its dimensions ($\boldsymbol{\alpha}$), spatial location ($\boldsymbol{\beta}$), and conductivity (σ_{r}) were treated as parameters to be estimated during the inversion process. In summary, a total of 10 parameters were used to define the physical model of the subsurface, represented by the vector $\mathbf{s} = [\boldsymbol{\alpha}, \boldsymbol{\beta}, \sigma_{\mathrm{r}}, \boldsymbol{\lambda}]$, where $\boldsymbol{\lambda} = [\lambda_1, \lambda_2, \lambda_3]$ represents the conductivities of the subsurface layers.

We used a FE grid of $114 \times 80 \times 60$ elements, representing a physical domain of 57 km $\times$50 km $\times$11 km, to compute the

accurate forward EM response (f^{acc}; Figure 5b). To implement the surrogate modeling with an approximate forward EM response (f^{app}), a coarser FE grid of $44 \times 32 \times 30$ elements was used (Figure 5c). Following the approach outlined in the synthetic example (Section 3.1.1), we generated a training database for the statistical model of discrepancies between the EM responses obtained from the accurate and approximate forward computations. Specifically, 20,000 realizations of the parametric subsurface model vector $\mathbf{s}$ were sampled from the prior distributions of each parameter as defined in Table 7. The complete computation of the database required 2.35 d using two nodes equipped with 128 processors and 66 GB of memory. On average, each run of the surrogate modeling took 3.1 s, whereas each run of the accurate forward computation required 57.8 s. After discarding the error samples $\boldsymbol{\xi}$ that did not exceed the measurement uncertainty at any point in the data vector, the resulting training database contained 19,886 samples.

Once the database established, the samples were reshaped into arrays of size 14×5 to be used in the training process of the generative network. Here, 14 corresponds to the maximum number of receivers required to incorporate the information for each of the five EM sources considered. Since the number of receivers is not the same for each source, a mask was applied to the matrix elements without data. Additionally, four channels were used to encode two frequencies, each with amplitude and phase. Due to the smaller and non-square size of the samples compared to the synthetic example, it was necessary to adapt the various components of the GAN architecture (summarized in Table 6) to suit this specific problem. For training, the database was normalized to the range $(-1, 1)$ by taking the maximum and minimum pointwise values, i.e. for each frequency in amplitude and phase, and for each source and receiver. The generative network was trained over eight thousand epochs, each consisting of 100 iterations using batches of 64 samples. The total training time was 7.75 hours on an A100GPU with 40 GB of memory.

After training, the statistical model enables us to represent the correction $\boldsymbol{\xi}$ of dimension 204 using a reduced number of parameters (only six) organized in the array $\mathbf{z}$ of size $3 \times 2 \times 1$. To assess the model's ability to capture the distribution of the original dataset, we compare the mean and standard deviation of the training database with those computed from a set of 19,886 fake samples generated by the network. Figure 6 shows this comparison, where the means are plotted as dots and the standard deviations are represented as error bars. A good agreement is observed between the two datasets across different components, both in amplitude and phase, for each source and frequency. Finally, we incorporate the trained statistical model as a correction in the inversion process by assigning a prior distribution

$\mathcal{U}(-1,1)$ to each parameter in the array $\mathbf{z}$ of the model. Additionally, we introduce a correction scale factor κ, which is also treated as a parameter with a prior distribution $\mathcal{U}(0,2)$.

Similar to the synthetic inversion (Section 3.1), we considered four inversion cases: using the approximate forward computation $\mathsf{f}^{\mathrm{app}}$ (1) without correction; (2) with scaled correction; (3) with delayed and scaled correction; and (4) using the accurate forward computation $\mathsf{f}^{\mathrm{acc}}$. In case (3), the application of the correction was delayed by eight thousand iterations. The inversion using $\mathsf{f}^{\mathrm{app}}$ and scaled correction converged after 97,890 iterations, which took 1.29 d. In contrast, the inversion using $\mathsf{f}^{\mathrm{app}}$ and delayed and scaled correction converged considerably faster, after 37,730 iterations in 17.05 h. Regarding the inversion using $\mathsf{f}^{\mathrm{app}}$ without correction, it showed rapid convergence, reaching a solution after 16,710 iterations in 4.92 h, due to the smaller number of parameters involved. A similar behavior is observed for the inversion using $\mathsf{f}^{\mathrm{acc}}$, which converged after 11,270 iterations. However, due to the use of a forward model that is accurate but computationally demanding, the total computation time was 2.67 d.

The aforementioned metrics are presented in Table 8, which also shows the total time required for each inversion, calculated by quadrupling the number of iterations necessary for convergence. We observe that incorporating the error correction leads to improved data misfit values. However, this improvement appears to result primarily from random error compensation—called overfitting—rather than from a more accurate representation of the EM data by the subsurface model. This may be because the neural network correction model introduces random variability that is not inherent to the rather smooth forward EM response.

Table 7 summarizes the most relevant statistical metrics of the marginal distributions of the subsurface model parameters. Additionally, Figure 7 compares these distributions in terms of the marginal posterior densities. Concerning the reservoir dimensions, a clear determination is not achieved in the y-direction, with significant differences observed across the different cases, possibly due to the sparse distribution of receivers along that direction. In particular, the use of the error correction reduces the estimated reservoir thickness, although not sufficiently when compared to the estimate obtained using the accurate forward computation. Regarding the reservoir position, the most notable differences appear in the depth estimate, especially between the $\mathsf{f}^{\mathrm{app}}$ case with scaled correction and the other variants. A similar pattern is observed for the conductivity parameter of the deepest layer, suggesting that, in this case, the correction helps to compensate for inaccuracies in the approximate forward computation by shifting the inversion

towards different regions of the parameter space. This behavior is consistent with the slower convergence observed for this particular inversion. In contrast, the f^{app} case with delayed and scaled correction, while not yielding substantially different estimates from the f^{app} case without correction in terms of parameters such as reservoir thickness and conductivity, appears to produce estimates more in line with those of the f^{acc} case, namely, a thinner and more resistive reservoir.

We now focus on assessing the presence of an oil reservoir based on the CSEM data inversion employing the accurate forward computation. Figures 8a and 8b present slices in the xz and xy planes, respectively, of the most likely model parameters derived from the posterior pdf. The inversion results suggest that the centroid of the resistive anomaly—interpreted as the reservoir rock with a certain degree of oil saturation—is most likely located at a depth of approximately 1.23 km below the seabed, nearly centered along line L1 in the y-direction, and around 9.65 km in the x-direction. The spatial uncertainty estimated from the posterior pdf indicates a variability of less than 1 km horizontally and a few meters vertically. Figure 8b shows the mean reservoir dimensions, together with the plus one standard deviation (dashed line), and minus one standard deviation (dash-dotted line) values according to our posterior pdf, providing a visual measure of the inferred variability in the reservoir geometry. The misfit of the most likely model parameters is 6.070 ± 0.001. Removing the resistive anomaly from the conductivity model increases the misfit to 6.59, indicating that the resistive body makes a significant contribution to the CSEM response reducing the data misfit.

From a prospecting perspective, the CSEM data inversion results obtained can be directly related to the net rock volume—defined as the portion of reservoir volume containing hydrocarbons—which is a major source of uncertainty in the estimation of recoverable reserves used in prospect risk analysis (Baltar & Roth, 2013). By computing the ellipsoidal anomaly volume for each sample in the posterior pdf, we obtained the marginal probability density function of the reservoir volume (Figure 8c). The most likely volume is 2.45×10^9 m^3, while the distribution mean of the volume plus (minus) its standard deviation is 2.60×10^9 m^3 (2.09×10^9 m^3). Although additional parameters are required to evaluate the volume of recoverable resources, the estimated net rock volume, combined with in situ measurements of rock properties, would provide valuable input for resource volume estimation if the presence of hydrocarbons were confirmed. As an illustrative example, following the formulation given by Gabrielsen et al. (2013), the net rock volume

can be converted into an estimated recoverable resource volume as:

$$V_{\text{res}} = \frac{V_{\text{net}}\varphi(1 - S_{\text{w}})\Gamma}{B_{\text{oil}}}, \tag{3.3}$$

where V_{net} is the net rock volume, φ is porosity, S_{w} is water saturation, Γ is the recovery factor, and B_{oil} is the oil formation volume factor. Assuming that the reservoir conductivity contrast is solely due to the presence of hydrocarbons, the partial saturation of formation water can be estimated using the resistivity index relationship $\text{IR} = R_{\text{t}}/R_0 = S_{\text{w}}^{-n}$, where R_{t} is the resistivity of the rock containing hydrocarbons, R_0 is the resistivity of the rock fully saturated with formation water, and n is the saturation exponent (commonly close to 2) (Mavko et al., 2009). Using the most likely conductivity values obtained from the inversion for the reservoir and for layer 2 (Table 7), and assuming $n = 2$, we estimate a water saturation of $S_{\text{w}} = 0.19$. Furthermore, Bruhn et al. (2017) reported that the porosity of siliciclastic turbidite reservoirs above the salt layer in the Campos Basin ranges between 15% and 30%; therefore, we adopt the conservative value $\varphi = 0.15$ for the resource estimation. In addition, Bruhn et al. (2017) noted that the oil found above the salt in the Campos Basin is heavy (13–17° API), suggesting a formation volume factor close to unity; hence, we take $B_{\text{oil}} = 1.2$. Similar to other reservoirs in Campos Basin, a recovery factor of $\Gamma = 0.4$ is assumed (e.g. Dumas et al., 2018). Using our most likely estimated volume of 2.45×10^9 m^3, the last parameters mentioned above, and equation (3.3), the corresponding recoverable resource volume is approximately 624 million barrels (MMbbl).

To assess whether the conductivity of layer 2 (10^{λ_2}) influences the estimation of the reservoir conductivity ($10^{\sigma_{\text{r}}}$), we examined the correlation between these parameters. The scatter plot in Figure 8d shows that the correlation is negligible, as indicated by a Pearson correlation coefficient of -0.1 (Myers & Well, 2003). Conversely, the scatter plot between the reservoir volume and the reservoir conductivity contrast ($10^{\lambda_2 - \sigma_{\text{r}}}$) in Figure 8e reveals a moderate negative correlation (Pearson correlation coefficient of -0.53). This relationship is physically consistent, as the amplitude of the anomalous EM field is jointly controlled, at least in part, by the conductivity contrast and the volume of the anomalous body. Consequently, a smaller body with a higher conductivity contrast can produce a response comparable to that of a larger body with a lower contrast.

4 | DISCUSSION

Using our performant parallelized forward solver, we were able to carry out 3D probabilistic inversion of CSEM data within an acceptable time frame of a few days, even in scenarios involving multiple sources. Our proposed methodology offers a straightforward and practical strategy for accelerating forward modeling without neglecting the inaccuracies introduced by the mesh coarsening process. Both the approximate forward computation and the statistical correction for modeling errors are designed to be computationally efficient and memory-conservative. This parallel forward capability is central to reduce computation times, while the use of multiple Markov chains running in parallel further improves the exploration of the parameter space and accelerates convergence to the posterior pdf (e.g. Blatter et al., 2021; Peng et al., 2024).

In the synthetic case study, the methodology successfully accelerates the inversion process while preserving the accuracy of the posterior pdf. In terms of reservoir geometry prediction, the inversion performance obtained with the approximate forward computation is clearly improved when the modeling error correction is applied compared to when it is ignored, situation also observed in the study by Levy et al. (2021). The use of the correction produces broader marginal distributions—reflecting greater flexibility in the inferred physical parameters—while still concentrating probability densities around the true values (Figure 4).

In the real CSEM data acquisition, even when accounting for modeling error, the inversion of the data remains challenging due to limited data coverage. The acquisition layout, consisting of measurements along two survey lines with in-line electric field data, forms the basis for constructing the statistical error model. However, this configuration appears insufficient to fully mitigate biases in the estimation of depth-sensitive parameters, such as reservoir thickness or conductivity contrast. Furthermore, we observe significant variability across inversion runs in the estimated reservoir extent along the direction perpendicular to line L1 (Figure 7). This inconsistency suggests that additional data coverage in this direction could substantially improve the robustness and reliability of the inversion results.

It is important to note that the presented inversion methodology involves a preliminary (offline) stage dedicated to the generation of the training dataset and the training of the generative neural network, which also entails a computational cost. In the field data inversion case, database generation was the most time-consuming task (taking approximately

2.35 d). However, this step was performed using two computing nodes, whereas the inversion stage was executed with five nodes. Assuming independent computation of each model, the preparatory stage could be reduced to less than half the demanded time if performed with the same computational resources as the inversion. Therefore, the preparatory stage does not significantly affect the overall runtime of the entire process. Moreover, in some scenarios, this stage could be incorporated into the early phases of the project development, such as during regional studies and feasibility assessments, prior to data acquisition. This approach also entails careful and cost-effective model parameterization tailored to the specific problem. Consequently, by the time measurements are acquired, or during subsequent acquisition phases, the pre-trained statistical model could already be available, enabling the delivery of preliminary interpretations derived from an effective 3D probabilistic inversion. In the discussed scenario, the benefits of the acceleration become especially evident when the modeling error correction is applied in a delayed fashion. This staged approach appears to enhance convergence by initially focusing the exploration on the physical model parameters and subsequently expanding it to account for modeling discrepancies.

It is becoming more widespread the use of probabilistic approaches for data inversion, especially in light of recent technological progress, most notably the increasing availability of computational resources and the rapid evolution of machine learning techniques. The growing development and application of sampling algorithms across various geoscientific techniques motivate our interest in applying them to the 3D probabilistic inversion of CSEM data. Nowadays, multiple strategies for sampling the posterior distribution are widely employed, including Sequential Monte Carlo (Doucet & Johansen, 2009), Parallel Tempering MCMC (Sambridge, 2013), Hamiltonian Monte Carlo (Neal, 2011), and Posterior Diffusion Sampling (Chung et al., 2024). Several of these approaches have already been tested in 2D MT inversion (e.g., Blatter et al., 2021; Peng et al., 2024), as well as in 1D and 2D CSEM inversion (e.g., Ray et al., 2014; Ray, 2021; Faghih et al., 2024), outlining a promising path toward fully 3D inversion. In addition, the adaptability and flexibility of machine learning data-driven systems demonstrate their potential to enhance the online inversion stage, where the system must assimilate new data while simultaneously exploring the parameter space. Recent contributions, such as the active learning framework proposed by Kapadia et al. (2024) in the context of parametric non-linear dynamical systems, exemplify this capacity. In that work, an error-estimator-based optimality criterion guides the active learning process, iteratively improving the accuracy of the surrogate model as the system evolves. In our own work,

we use strategic developments in this direction by incorporating generative neural networks as a parametric model trained during the offline phase and jointly inverted with the physical model parameters during the online phase.

5 | CONCLUSIONS

We have presented a workflow for 3D probabilistic inversion of Controlled-Source Electro-Magnetic (CSEM) data that achieves good performance within practical computation times. The approach addresses the high computational demands of CSEM forward modeling by introducing a surrogate model based on a mesh coarsening strategy. To further account for the modeling error introduced by this approximation, we employed deep learning techniques to construct a parametric correction model. This allows the inversion process to simultaneously estimate subsurface physical parameters and correction terms, thereby improving accuracy while maintaining computational efficiency. The methodology was validated through a synthetic 3D marine CSEM experiment, where the probabilistic inversion successfully recovered the true subsurface parameters. The results demonstrated that incorporating the correction model improves predictive performance compared to neglecting it, while also providing significant computational savings relative to the accurate forward computation. Finally, the application to field data enabled the characterization of the subsurface and the estimation of the location and geometry of a hydrocarbon reservoir. The achieved computation times are acceptable for a 3D probabilistic inversion framework, even in the presence of multiple sources.

references

Allabou, M., Bouclier, R., Garambois, P., & Monnier, J., 2024. Reduction of the shallow water system by an error aware pod-neural network method: Application to floodplain dynamics, *Computer Methods in Applied Mechanics and Engineering*, **428**, 117094.

Arjovsky, M., Chintala, S., & Bottou, L., 2017. Wasserstein generative adversarial networks, in *Proceedings of the 34th International Conference on Machine Learning*, vol. 70, pp. 214–223.

Attias, E., Weitemeyer, K., Hölz, S., Naif, S., Minshull, T. A., Best, A. I., Haroon, A., Jegen-Kulcsar, M., & Berndt, C., 2018. High-resolution resistivity imaging of marine gas hydrate structures by combined inversion of CSEM towed and ocean-bottom receiver data, *Geophysical Journal International*, **214**(3), 1701–1714.

Bajpai, A., Singh, A., & Varma, S., 2025. Hierarchical transdimensional bayesian inversion of 2D magnetotelluric data, *GEOPHYSICS*, **90**(3), WA247–WA260.

Baltar, D. & Roth, F., 2013. Reserves estimation methods for prospect evaluation with 3D CSEM data, *First Break*, **31**, 103–110.

Barker, N., 2004. *Electromagnetic investigation of the Lucky Strike Seamount near 37°N, Mid-Atlantic Ridge*, Ph.D. thesis, University of Southampton, Southampton, England.

Berryman, J. G., 1995. *Mixture Theories for Rock Properties*, pp. 205–228, American Geophysical Union (AGU).

Blatter, D., Key, K., Ray, A., Gustafson, C., & Evans, R., 2019. Bayesian joint inversion of controlled source electromagnetic and magnetotelluric data to image freshwater aquifer offshore new jersey, *Geophysical Journal International*, **218**(3), 1822–1837.

Blatter, D., Ray, A., & Key, K., 2021. Two-dimensional bayesian inversion of magnetotelluric data using trans-dimensional gaussian processes, *Geophysical Journal International*, **226**, 548–563.

Bruhn, C., Pinto, A., Johann, P., Branco, C., Salomão, M., & Freire, E., 2017. Campos and Santos Basins: 40 years of reservoir characterization and management of shallow- to ultra-deep water, post- and pre-salt reservoirs - Historical overview and future challenges.

Castillo-Reyes, O., Queralt, P., Marcuello, A., & Ledo, J., 2021. Land CSEM simulations and experimental test using metallic casing in a geothermal exploration context: Vallès basin (ne spain) case study, *IEEE Transactions on Geoscience and Remote Sensing*, **60**, 1–13.

Christensen, N. & Dodds, K., 2007. 1D inversion and resolution analysis of marine CSEM data, *Geophysics*, **72**, WA27–WA38.

Chung, H., Kim, J., Mccann, M. T., Klasky, M. L., & Ye, J. C., 2024. Diffusion posterior sampling for general noisy inverse problems.

Constable, S., 2006. Marine electromagnetic methods—A new tool for offshore exploration, *The Leading Edge*, **25**(4), 438–444.

Coppo, N., Darnet, M., Harcouet-Menou, V., Wawrzyniak, P., Manzella, A., Bretaudeau, F., Romano, G., Lagrou, D., & Girard, J.-F., 2016. Characterization of Deep Geothermal Energy Resources in Low enthalpy sedimentary basins in Belgium using Electro-Magnetic Methods – CSEM and MT results, in *European Geothermal Congress 2016*, Strasbourg, France.

Corseri, R., Seillé, H., Faleide, J. I., Planke, S., Senger, K., Abdelmalak, M. M., Gelius, L. J., Mohn, G., & Visser, G., 2024. Deep basin conductor characterization using machine learning-assisted magnetotelluric bayesian inversion in the sw barents sea, *Geophysical Journal International*, **238**(1), 420–432.

Creswell, A., White, T., Dumoulin, V., Arulkumaran, K., Sengupta, B., & Bharath, A. A., 2018. Generative adversarial networks: An overview, *IEEE Signal Processing Magazine*, **35**(1), 53–65.

Darnet, M., Wawrzyniak, P., Coppo, N., Nielsson, S., Schill, E., & Fridleifsson, G., 2020. Monitoring geothermal reservoir developments with the Controlled-Source Electro-Magnetic method — A calibration study on the Reykjanes geothermal field, *Journal of Volcanology and Geothermal Research*, **391**, 106437.

De Pasquale, G. & Linde, N., 2017. On structure-based priors in bayesian geophysical inversion, *Geophysical Journal International*, **208**, 1342–1358.

Doucet, A. & Johansen, A., 2009. A tutorial on particle filtering and smoothing: Fifteen years later, *Handbook of Nonlinear Filtering*, **12**.

Dramsch, J. S., 2020. Chapter one - 70 years of machine learning in geoscience in review, in *Machine Learning in Geosciences*, vol. 61 of **Advances in Geophysics**, pp. 1–55.

Dumas, G. E. S., Freire, E. B., Johann, P. R. S., Silva, L. S., Vieira, R. A. B., Bruhn, C. H. L., & Pinto, A. C. C., 2018. Reservoir management of the Campos Basin brown fields, **Offshore Technology Conference**, D021S018R004.

Dunham, M. W., Ansari, S., & Farquharson, C. G., 2018. Application of 3D marine controlled-source electromagnetic finite-element forward modeling to hydrocarbon exploration in the Flemish Pass Basin offshore Newfoundland, Canada, *GEOPHYSICS*, **83**(2), WB33–WB49.

Elías, M. W., Zyserman, F. I., Rosas-Carbajal, M., & Manassero, M. C., 2021. Three-dimensional modelling of controlled source electro-magnetic surveys using non-conforming finite element methods, *Geophysical Journal International*, **229**(2), 1133–1151.

Ettayebi, M., Wang, S., & Landrø, M., 2023. Time-lapse 3D CSEM for reservoir monitoring based on rock physics simulation of the wisting oil field offshore norway, *Sensors*, **23**(16), 7197.

Faghih, Z., Haroon, A., Jegen, M., Gehrmann, R., Schwalenberg, K., Micallef, A., Dettmer, J., Berndt, C., Mountjoy, J., & Weymer, B. A., 2024. Characterizing offshore freshened groundwater salinity patterns using trans-dimensional bayesian inversion of controlled source electromagnetic data: A case study from the canterbury bight, new zealand, *Water Resources Research*, **60**(3), e2023WR035714.

Fuhg, J., 2019. *Adaptive surrogate modeling for parametric studies with Kriging*, Ph.D. thesis, Leibniz Universität Hannover, Hannover, Germany.

Gabrielsen, P. T., Abrahamson, P., Panzner, M., Fanavoll, S., & Ellingsrud, S., 2013. Exploring frontier areas using 2D seismic and 3D CSEM data, as exemplified by multi-client data over the skrugard and havis discoveries in the barents sea, *First Break*, **31**, 63–71.

Gehrmann, R. A. S., Dettmer, J., Schwalenberg, K., Engels, M., Dosso, S. E., & Özmaral, A., 2015. Trans-dimensional bayesian inversion of controlled-source electromagnetic data in the german north sea, *Geophysical Prospecting*, **63**(6), 1314–1333.

Gehrmann, R. A. S., North, L. J., Graber, S., Szitkar, F., Petersen, S., Minshull, T. A., & Murton, B. J., 2019. Marine mineral exploration with controlled source electromagnetics at the tag hydrothermal field, 26°n mid-atlantic ridge, *Geophysical Research Letters*, **46**(11), 5808–5816.

Gelman, A., Rubin, D. B., et al., 1992. Inference from iterative simulation using multiple sequences, *Statistical science*, **7**(4), 457–472.

Goodfellow, I., Bengio, Y., & Courville, A., 2016. *Deep Learning*, MIT Press.

Grayver, A., Streich, R., & Ritter, O., 2014. 3-D inversion and resolution analysis of land-based CSEM data from the Ketzin CO_2 storage formation, *Geophysics*, **79**(2), E101–E114.

Gustafson, C., Key, K., & Evans, R., 2019. Aquifer systems extending far offshore on the u.s. atlantic margin, *Scientific Reports*, **9**, 8709.

Hansen, T., Cordua, K., Jacobsen, B., & Mosegaard, K., 2014. Accounting for imperfect forward modeling in geophysical inverse problems - exemplified for crosshole tomography, *Geophysics*, **79**, H1–H21.

He, K., Zhang, X., Ren, S., & Sun, J., 2015. Delving deep into rectifiers: Surpassing human-level performance on imagenet classification, in *2015 IEEE International Conference on Computer Vision (ICCV)*, pp. 1026–1034.

He, K., Zhang, X., Ren, S., & Sun, J., 2016. Deep residual learning for image recognition, in *Deep Residual Learning for Image Recognition*, pp. 770–778.

Hölz, S., Swidinsky, A., Sommer, M., Jegen, M., & Bialas, J., 2015. The use of rotational invariants for the interpretation of marine CSEM data with a case study from the north alex mud volcano, west nile delta, *Geophysical Journal International*, **201**(1), 224–245.

Ishizu, K. & Ogawa, Y., 2021. Offshoreonshore resistivity imaging of freshwater using a controlled source electromagnetic method: A feasibility study, *GEOPHYSICS*, **86**, 1–55.

Ishizu, K., Ogawa, Y., Tseng, K. H., Kunitomo, T., Kitaoka, N., Caldwell, G., Minami, T., Serita, S., Ichihara, H., Bertrand, E., & Heise, W., 2024. Controlled-source electromagnetic survey in a volcanic area: relationship between stacking time and signal-to-noise ratio and comparison with magnetotelluric data, *Geophysical Journal International*, **240**.

Jetchev, N., Bergmann, U., & Vollgraf, R., 2017. Texture synthesis with spatial generative adversarial networks, *arXiv*, p. 1611.08207.

Kapadia, H., Feng, L., & Benner, P., 2024. Active-learning-driven surrogate modeling for efficient simulation of parametric nonlinear systems, *Computer Methods in Applied Mechanics and Engineering*, **419**, 116657.

Köpke, C., Irving, J., & Elsheikh, A. H., 2018. Accounting for model error in bayesian solutions to hydrogeophysical inverse problems using a local basis approach, *Advances in Water Resources*, **116**, 195–207.

Köpke, C., Irving, J., & Roubinet, D., 2019. Stochastic inversion for soil hydraulic parameters in the presence of model error: An example involving ground-penetrating radar monitoring of infiltration, *Journal of Hydrology*, **569**, 829–843.

Laloy, E. & Vrugt, J. A., 2012. High-dimensional posterior exploration of hydrologic models using multiple-try dream (zs) and high-performance computing, *Water Resources Research*, **48**(1).

Levy, S., Hunziker, J., Laloy, E., Irving, J., & Linde, N., 2021. Using deep generative neural networks to account for model errors in Markov chain Monte Carlo inversion, *Geophysical Journal International*, **228**(2), 1098–1118.

Li, K., Li, Y., Li, L., & Lanteri, S., 2023. Surrogate modeling of time-domain electromagnetic wave propagation via dynamic mode decomposition and radial basis function, *Journal of Computational Physics*, **491**, 112354.

Li, P., Du, Z., Li, Y., & Wang, J., 2024. One-dimensional deep learning inversion of marine controlled-source electromagnetic data, *Geophysical Prospecting*, **73**(1), 397–417.

Liu, W., Wang, H., Xi, Z.-z., Zhang, R., & Huang, X., 2022. Physics-driven deep learning inversion with application to magnetotelluric, *Remote Sensing*, **14**(13), 3218.

Liu, X., Craven, J., Tschirhart, V., & Grasby, S., 2024. Estimating three-dimensional resistivity distribution with magnetotelluric data and a deep learning algorithm, *Remote Sensing*, **16**, 3400.

Luo, W., Chen, X., Wang, S., Zhao, S., Yin, X., Lan, X., Jiang, P., & Wang, S., 2024. Deep learning-based near-field effect correction method for controlled source electromagnetic method and application, *PLOS ONE*, **19**(11), 1–21.

Maas, A. L., Hannun, A. Y., & Ng, A. Y., 2013. Rectifier nonlinearities improve neural network acoustic models, in *Proceedings of the 30th International Conference on Machine Learning*, vol. 28,3.

Manassero, M., Afonso, J., Zyserman, F., Zlotnik, C., & Fomin, I., 2020. A Reduced Order Approach for Probabilistic Inversions of 3D magnetotelluric data I: General Formulation, *Geophysical Journal International*, **223**(3), 1837–1863.

Mavko, G., Mukerji, T., & Dvorkin, J., 2009. *The rock physics handbook: Tools for seismic analysis of porous media*, Cambridge University Press, The Pitt Building, Trumpington Street, Cambridge CB2 IRP, United Kingdom.

Menke, W., 1989. *Geophysical Data Analysis: Discrete Inverse Theory*, vol. 45 of **International Geophysics Series**, Academic Press.

Mörbe, W., 2020. *Deep Controlled Source Electromagnetics for Mineral Exploration: A Multidimensional Validation Study in Time and Frequency Domain*, Ph.D. thesis, Universität zu Köln, Köln, Germany.

Mosegaard, K. & Tarantola, A., 1995. Monte carlo sampling of solutions to inverse problems, *Journal of Geophysical Research: Solid Earth*, **100**(B7), 12431–12447.

Myers, J. & Well, A., 2003. *Research Design and Statistical Analysis*, Lawrence Erlbaum Associates.

Neal, R., 2011. *MCMC using Hamiltonian dynamics*, chap. 5, Chapman and Hall/CRC.

Pan, K., Ling, W., Zhang, J., Zhong, X., Ren, Z., Hu, S., He, D., & Tang, J., 2023. MT2DInv-Unet: A two-dimensional magnetotelluric inversion method based on deep learning technology, *GEOPHYSICS*, **89**, 1–61.

Peng, R., Han, B., Hu, X., Li, J., & Liu, Y., 2024. 2-d probabilistic inversion of MT data and uncertainty quantification using the hamiltonian monte carlo method, *Geophysical Journal International*, **237**(3), 1826–1841.

Penz, S., Duchêne, B., & Mohammad-Djafari, A., 2017. Variational bayesian inversion of 3D CSEM geophysical data, *GEOPHYSICS*, **83**, 1–50.

Price, K., Storn, R., & Lampinen, J., 2005. *Differential Evolution-A Practical Approach to Global Optimization*, vol. 141.

Puzyrev, V., 2019. Deep learning electromagnetic inversion with convolutional neural networks, *Geophysical Journal International*, **218**, 817–832.

Ray, A., 2021. Bayesian inversion using nested trans-dimensional gaussian processes, *Geophysical Journal International*, **226**(1), 302–326.

Ray, A. & Myer, D., 2019. Bayesian geophysical inversion with trans-dimensional gaussian process machine learning, *Geophysical Journal International*, **217**, 1706–1726.

Ray, A., Key, K., Bodin, T., Myer, D., & Constable, S., 2014. Bayesian inversion of marine CSEM data from the scarborough gas field using a transdimensional 2-d parametrization, *Geophysical Journal International*, **199**(3), 1847–1860.

Rosas-Carbajal, M., Linde, N., Kalscheuer, T., & Vrugt, J. A., 2013. Two-dimensional probabilistic inversion of plane-wave electromagnetic data: methodology, model constraints and joint inversion with electrical resistivity data, *Geophysical Journal International*, **196**(3), 1508–1524.

Rosas-Carbajal, M., Linde, N., Peacock, J., Zyserman, F., Kalscheuer, T., & Thiel, S., 2015. Probabilistic three-dimensional time-lapse inversion of magnetotelluric data to infer mass transfer in a geothermal system, *Geophys. J. Int.*, **203**(3), 1946–1960.

Sambridge, M., 2013. A parallel tempering algorithm for probabilistic sampling and multimodal optimization, *Geophysical Journal International*, **196**(1), 357–374.

Schaller, A., Streich, R., Drijkoningen, G., Ritter, O., & Slob, E., 2017. A land-based CSEM method for oil field exploration: An example from the schoonebeek oil field, *GEOPHYSICS*, **83**, 1–71.

Schwalenberg, K., Rippe, D., Koch, S., & Scholl, C., 2017. Marine-controlled source electromagnetic study of methane seeps and gas hydrates at opouawe bank, hikurangi margin, new zealand, *Journal of Geophysical Research: Solid Earth*, **122**(5), 3334–3350.

Seillé, H. & Visser, G., 2020. Bayesian inversion of magnetotelluric data considering dimensionality discrepancies, *Geophysical Journal International*, **223**(3), 1565–1583.

Sheen, D., 1997. Approximation of electromagnetic fields: Part I. continuous problems, *SIAM J. Appl. Math.*, **57**, 1716–1736.

Signorini, M., Zlotnik, S., & Díez, P., 2017. Proper generalized decomposition solution of the parameterized helmholtz problem: application to inverse geophysical problems, *International Journal for Numerical Methods in Engineering*, **109**(8), 1085–1102.

Singh, A. & Dehiya, R., 2025. 3D inversion scheme for high-resolution analysis of continental scale magnetotelluric data, *ESS Open Archive*.

Streich, R., 2016. Controlled-source electromagnetic approaches for hydrocarbon exploration and monitoring on land, *Surveys in Geophysics*, **37**(1), 47–80.

Streich, R., M., B., & Ritter, O., 2013. Robust processing of noisy land-based controlled-source electromagnetic data, *GEOPHYSICS*, **78**(5), E237–E247.

Subramanian, A. K. & Chong, N. Y., 2019. Mean spectral normalization of deep neural networks for embedded automation, *arXiv*, p. 1907.04003.

Tarantola, A., 2005. *Inverse problem theory and methods for model parameter estimation*, vol. 89, siam.

Tarantola, A. & Valette, B., 1982. Inverse problems= quest for information, *Journal of Geophysics*, **50**, 150–170.

ter Braak, C. & Vrugt, J., 2008. Differential evolution markov chain with snooker updater and fewer chains, *cs and Computing*, **18**(4), 435–446.

Thorkildsen, V. & Gelius, L.-J., 2023. Electromagnetic resolution - a CSEM study based on the wisting oil field, *Geophysical Journal International*, **233**, 2124–2141.

Tveit, S., Mannseth, T., Park, J., Sauvin, G., & Agersborg, R., 2020. Combining CSEM or gravity inversion with seismic avo inversion, with application to monitoring of large-scale co2 injection, *Computational Geosciences*, **24**, 1202–1220.

Ulyanov, D., Vedaldi, A., & Lempitsky, V., 2017. Improved texture networks: Maximizing quality and diversity in feed-forward stylization and texture synthesis, *arXiv*, p. 1701.02096.

Vrugt, J., 2015. *Manual of DREAM - accepted for publication in Environmental Modeling and Software*.

Vrugt, J., ter Braak, C., Diks, C., Robinson, B., Hyman, J., & Higdon, D., 2009. Accelerating Markov chain Monte Carlo simulation by Differential Evolution with Self-Adaptive Randomized Subpace Sampling, *International Journal of Nonlinear Sciences and Numerical Simulation*, **10**(3), 273–290.

Ward, S. & Hohmann, G. W., 1987. Electromagnetic theory for geophysical applications, in *Electromagnetic Methods in Applied Geophysics*, vol. 1 of **SEG Investigations in Geophysics 3**, ed. Nabiguian, M. N., SEG.

Wibawa, A., Putra Utama, A. B., Elmunsyah, H., Pujianto, U., Dwiyanto, F., & Hernandez, L., 2022. Time-series analysis with smoothed convolutional neural network, *Journal of Big Data*, **9**, 44.

Wu, X., Xue, G.-q., Zhao, Y., lv, P., Zhou, Z., & Shi, J., 2022. A deep learning estimation of the earth resistivity model for the airborne transient electromagnetic observation, *Journal of Geophysical Research: Solid Earth*, **127**(3), e2021JB023185.

Xiao, D., 2019. Error estimation of the parametric non-intrusive reduced order model using machine learning, *Computer Methods in Applied Mechanics and Engineering*, **355**, 513–534.

Yao, H., Ren, Z., Tang, J., Guo, R., & Yan, J., 2023. Trans-dimensional Bayesian joint inversion of magnetotelluric and geomagnetic depth sounding responses to constrain mantle electrical discontinuities, *Geophysical Journal International*, **233**(3), 1821–1846.

Yu, N., Ji, M., Zhang, C., Ye, Y., & Zhou, W., 2024. A novel frequency-division deep learning approach for magnetotelluric data quality enhancement, *GEOPHYSICS*, **90**, 1–86.

Yu, S. & Ma, J., 2021. Deep learning for geophysics: Current and future trends, *Reviews of Geophysics*, **59**(3), e2021RG000742.

Zhang, L., Ren, Z., Xiao, X., Tang, J., & Li, G., 2022. Identification and suppression of magnetotelluric noise via a deep residual network, *Minerals*, **12**, 766.

TABLE 1 Architecture of the 2D GAN model. The generator G progressively upsamples a low-dimensional spatial noise tensor into a multi-channel output using transposed convolutions (Trans. Conv.) with PReLU activation function and Instance Normalization (INorm) for each layer except the last one, which only uses transposed convolution with hyperbolic tangent. The critic D applies Spectral Normalization (SN) after a convolution (Conv.) operation, Mean Spectral Normalization (MSN) and LeakyReLU activation function for each layer except the last one, which only use SN after a convolution operation. Kernel size, stride, and padding are indicated for each layer, along with the corresponding output tensor dimensions.

Model	Layer	Filters	Kernel	Stride	Padding	Output size	Operation
Generator (G)	Input	-	-	-	-	$4 \times 4 (\times 1)$	-
	Layer 1	512	5	2	3	$5 \times 5 (\times 512)$	Trans. Conv., PReLU, INorm
	Layer 2	256	5	2	3	$7 \times 7 (\times 256)$	Trans. Conv., PReLU, INorm
	Layer 3	128	5	2	3	$11 \times 11 (\times 128)$	Trans. Conv., PReLU, INorm
	Layer 4	12	6	2	5	$16 \times 16 (\times 12)$	Trans. Conv., Tanh
Critic (D)	Input	-	-	-	-	$16 \times 16 (\times 12)$	-
	Layer 1	64	5	2	3	$9 \times 9 (\times 64)$	SN(Conv.), MSN, LeakyReLU
	Layer 2	256	5	2	3	$6 \times 6 (\times 256)$	SN(Conv.), MSN, LeakyReLU
	Layer 3	512	5	2	3	$4 \times 4 (\times 512)$	SN(Conv.), MSN, LeakyReLU
	Layer 4	12	1	2	0	$2 \times 2 (\times 12)$	SN(Conv.)

TABLE 2 Prior distributions, true values, and statistical metrics of the inversion results. Prior distributions for the shape and position of the resistive anomaly used in the inversion and in the generation of the training database for the synthetic example. The true values used to generate the synthetic data, along with the mode, mean, and standard deviation of the marginal distributions of the posterior pdfs obtained from the different inversion cases.

Parameter	Prior	True val.	f^{app} without corr.			f^{app} with scaled corr.			f^{app} delayed and scaled corr.			f^{acc}		
			Mode	Mean	Std. Dev.	Mode	Mean	Std. Dev.	Mode	Mean	Std. Dev.	Mode	Mean	Std. Dev.
α_1 (x) [km]	$\mathcal{U}(0.4, 6.6)$	4.52	5.66	5.81	0.32	4.44	4.59	0.30	4.44	4.43	0.21	4.84	5.00	0.32
α_2 (y) [km]	$\mathcal{U}(0.4, 6.6)$	2.14	2.03	2.18	0.12	2.24	2.33	0.21	2.13	2.24	0.13	2.05	2.20	0.15
α_3 (z) [km]	$\mathcal{U}(0.07, 0.22)$	0.22	0.073	0.13	0.039	0.073	0.15	0.044	0.16	0.17	0.033	0.073	0.14	0.048
β_1 (x) [km]	$\mathcal{U}(12.97, 18.97)$	13.52	13.82	13.66	0.10	13.46	13.30	0.11	13.13	13.28	0.10	13.60	13.52	0.05
β_2 (y) [km]	$\mathcal{U}(12.97, 18.97)$	17.88	17.86	18.01	0.11	18.13	18.04	0.11	18.02	18.02	0.10	17.79	17.88	0.05
β_3 (z) [km]	$\mathcal{U}(3.91, 5.90)$	5.27	5.22	5.19	0.038	5.33	5.32	0.041	5.32	5.32	0.045	5.26	5.25	0.031

TABLE 3 Metrics of the computational resources required to construct the database. The regular grid employed for computing the EM response with the accurate forward computation (f^{acc}) consists of $80 \times 80 \times 40$ elements, whereas the approximate forward computation (f^{app}) uses a coarser discretization of $40 \times 40 \times 24$ elements.

Forward	Samples	CPU procs.	Memory	Time	Frequency
f^{acc} and f^{app}	32,000	128	30 GB	2 d 3 h 25 min	1., 0.5, 0.25, 0.05 Hz
f^{acc}	1	4	-	$\sim$ 30 s	0.05 Hz
f^{app}	1	4	-	$\sim$ 3 s	0.05 Hz

TABLE 4 Performance metrics of the inversion of the synthetic data. Four cases were considered, using the approximate (f^{app}) and the accurate (f^{acc}) forward computation. Each f^{app} case specifies whether the correction was applied to the forward or not. The implementation of the approximate forward computation leads to a reduction in computational time of approximately one-third relative to the use of the accurate forward computation.

	f^{app} **without corr.**	f^{app} **with scaled corr.**	f^{app} **delayed and scaled corr.**	f^{acc}
Convergence time	4 h 13 min	10 h 7 min	9 h 14 min	25 h 43 min
Acceptance rate [%]	20.2	21.2	22.6	14.4
Misfit	1.024	1.012	1.012	1.007
Total time	16 h 52 min	1 d 16 h 49 min	1 d 14 h 40 min	4 d 15 h 24 min

TABLE 5 Absolute noise level (a) and source-receiver offset threshold (R) beyond which the phase information is no longer considered reliable, as a function of the frequency employed to define the measurement error model.

Frequency [Hz]	a [V/A/m^2]	R [km]
0.25	7×10^{-16}	8.0
0.5	3×10^{-16}	7.0
0.75	8×10^{-16}	6.7
1.5	5×10^{-16}	4.4

TABLE 6 Architecture of the 2D GAN model for the data field example. The generator G progressively upsamples a low-dimensional spatial noise tensor into a multi-channel output using transposed convolutions (Trans. Conv.) with PReLU activation function and Instance Normalization (INorm) for each layer, except the last one, which only uses a transposed convolution with hyperbolic tangent. The critic D applies Spectral Normalization (SN) after a convolution (Conv.) operation, Mean Spectral Normalization (MSN) and LeakyReLU activation function for each layer, except the last one, which only uses SN after a convolution operation. Kernel size, stride, and padding are indicated for each layer, along with the corresponding output tensor dimensions.

Model	Layer	Filters	Kernel	Stride	Padding	Output size	Operation
Generator (G)	Input	-	-	-	-	$3 \times 2 (\times 1)$	-
	Layer 1	512	(3,3)	(1,2)	(1,1)	$5 \times 2 (\times 512)$	Trans. Conv., PReLU, INorm
	Layer 2	256	(3,3)	(2,2)	(1,1)	$8 \times 3 (\times 256)$	Trans. Conv., PReLU, INorm
	Layer 3	128	(3,3)	(2,1)	(1,0)	$11 \times 5 (\times 128)$	Trans. Conv., PReLU, INorm
	Layer 4	4	(3,4)	(1,1)	(1,0)	$14 \times 5 (\times 4)$	Trans. Conv., Tanh
Critic (D)	Input	-	-	-	-	$14 \times 5 (\times 4)$	-
	Layer 1	64	(3,3)	(2,2)	(2,2)	$9 \times 9 (\times 64)$	SN(Conv.), MSN, LeakyReLU
	Layer 2	256	(3,3)	(2,2)	(2,2)	$6 \times 6 (\times 256)$	SN(Conv.), MSN, LeakyReLU
	Layer 3	512	(3,3)	(2,2)	(2,2)	$4 \times 4 (\times 512)$	SN(Conv.), MSN, LeakyReLU
	Layer 4	4	(3,3)	(2,2)	(1,1)	$2 \times 2 (\times 4)$	SN(Conv.)

TABLE 7 Prior distributions and statistical metrics of the inversion results. Prior distributions of the ten parameters used to describe the subsurface model, along with the mean, standard deviation, and mode of the marginal distributions of the posterior pdfs obtained from the different CSEM data field inversion cases.

Parameter	Prior	f^{app} without corr.			f^{app} with scaled corr.			f^{app} delayed and scaled corr.			f^{acc}		
		Mode	Mean	Std. Dev.	Mode	Mean	Std. Dev.	Mode	Mean	Std. Dev.	Mode	Mean	Std. Dev.
α_1 (x) [km]	$\mathcal{U}(0.37, 6.0)$	6.	6.	0.02	6.	6.	0.02	6.	6.	0.01	6.	6.	0.05
α_2 (y) [km]	$\mathcal{U}(0.50, 7.8)$	4.9	5.5	0.7	4.9	4.9	0.4	7.	7.	0.3	5.8	5.5	0.7
α_3 (z) [km]	$\mathcal{U}(0.09, 0.4)$	0.223	0.223	0.003	0.219	0.218	0.002	0.217	0.217	0.002	0.134	0.134	0.001
β_1 (x) [km]	$\mathcal{U}(-0.69, 25.7)$	9.44	9.48	0.102	9.13	9.23	0.069	9.21	9.22	0.059	9.65	9.53	0.114
β_2 (y) [km]	$\mathcal{U}(-11.8, 6.4)$	0.17	0.37	0.23	0.30	0.20	0.12	0.27	0.32	0.18	0.28	0.32	0.20
β_3 (z) [km]	$\mathcal{U}(3.68, 5.70)$	3.93	3.93	0.013	3.78	3.79	0.019	3.93	3.93	0.025	3.93	3.93	0.003
σ_r [log S/m]	$\mathcal{U}(-2., -1.)$	-1.004	-1.028	0.02	-1.001	-1.006	0.006	-1.053	-1.048	0.016	-1.321	-1.309	0.026
λ_1 [log S/m]	$\mathcal{U}(-2., 0.30)$	-0.116	-0.116	0.001	-0.116	-0.116	0.001	-0.115	-0.115	0.001	-0.117	-0.116	0.001
λ_2 [log S/m]	$\mathcal{U}(-2., 0.30)$	0.117	0.118	0.011	0.161	0.161	0.01	0.102	0.106	0.013	0.133	0.129	0.012
λ_3 [log S/m]	$\mathcal{U}(-2., 0.30)$	-2.	-1.708	0.223	0.248	0.09	0.203	-1.174	-1.239	0.38	-1.953	-1.714	0.20

TABLE 8 Data field inversion performance metrics. In the columns, the four inversion cases. The approximate forward computation (f^{app}) with scaled correction case exhibits slower convergence than the f^{app} with delayed and scaled correction case. The latter presents a substantial reduction in the total inversion time when compared to the accurate forward computation (f^{acc}) case.

	f^{app} **without corr.**	f^{app} **with scaled corr.**	f^{app} **delayed and scaled corr.**	f^{acc}
Convergence time	4 h 55 min	1 d 6 h 14 min	17 h 3 min	2 d 16 h 1 min
Acceptance rate [%]	16.8	12.2	6.6	22.2
Misfit	6.072	5.83	5.81	6.070
Total time	19 h 40 min	5 d 4 h 38 min	2 d 12 h 52 min	7 d 13 h 48 min

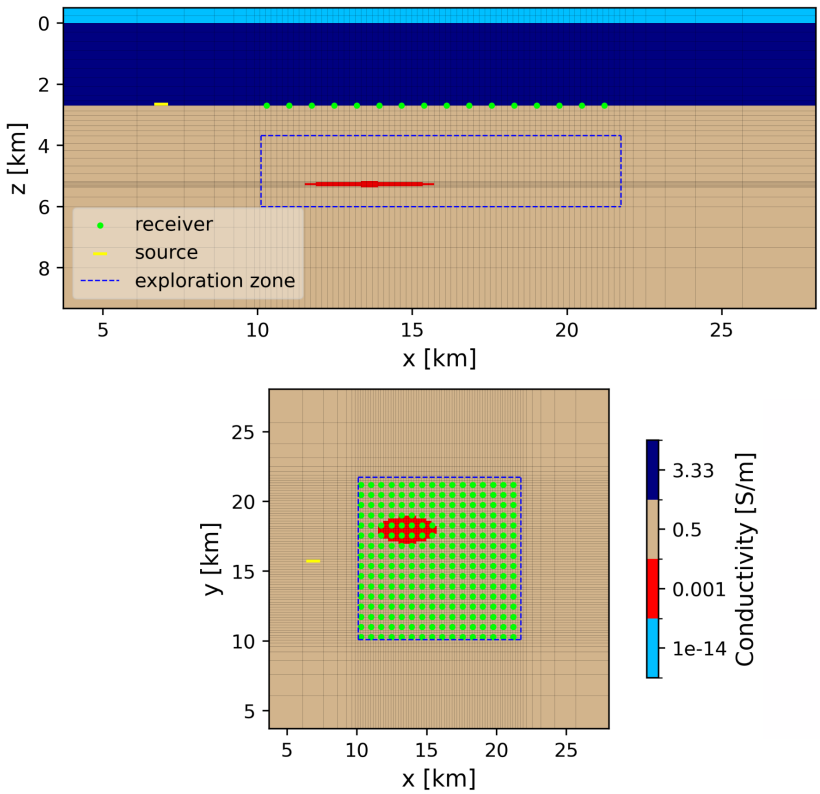

FIGURE 1 Synthetic model used for testing our inversion methodology. The horizontal electric dipole source (yellow line) is 50 m above the seafloor. An array of 16×16 receivers is used (green dots). The delineated exploration zone (blue dashed line) shows the limits where a resistive body (red silhouette) is proposed during the inversion.

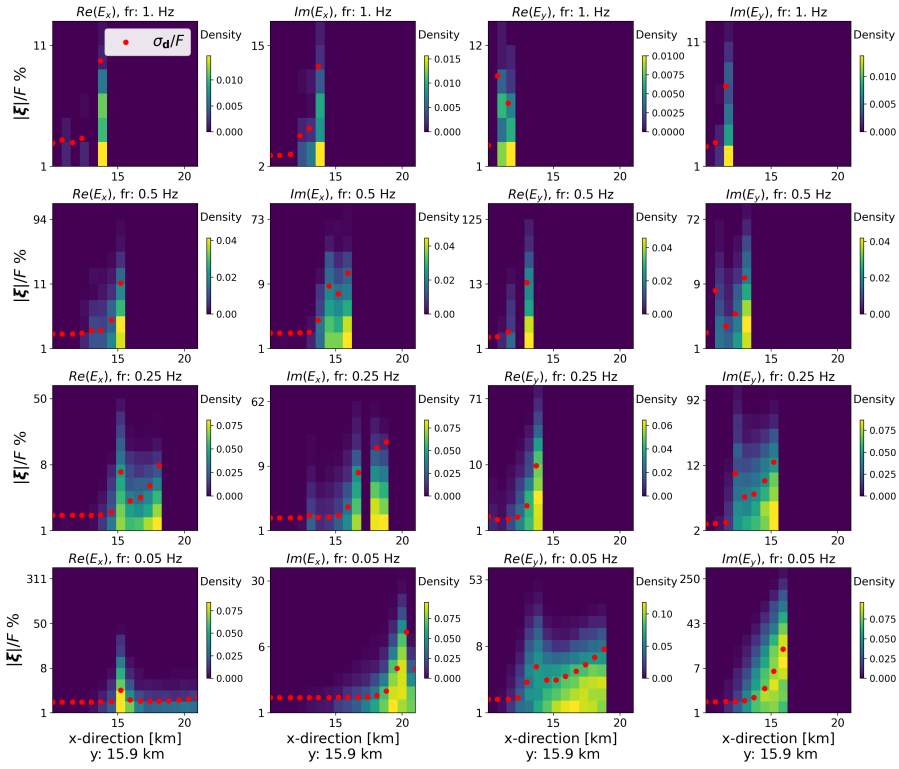

FIGURE 2 Density histograms of the absolute value of each sample $\boldsymbol{\xi}$ across the entire database (32,000 samples), represented using a color map. The title of each panel indicates the selected channel (or component) of the sample, that is, the electric field in the x or y direction, its real or imaginary part, and the corresponding frequency. The horizontal axis represents the components associated with the xy-positions of the receiver array. The vertical axis shows the percentage, on a logarithmic scale, of the absolute value of $\boldsymbol{\xi}$ relative to the observed data amplitude F, component-wise. Also, the synthetic data errors $\sigma_{\mathbf{d}}$ relative to F, component-wise, are displayed as red dots. Thus, in any given panel, the title identifies the channel, the horizontal axis corresponds to a specific receiver, the vertical axis to a percentage level relative to the observed data amplitude, and the color indicates the number of samples—out of the full database—that satisfy that particular combination of receiver and percentage.

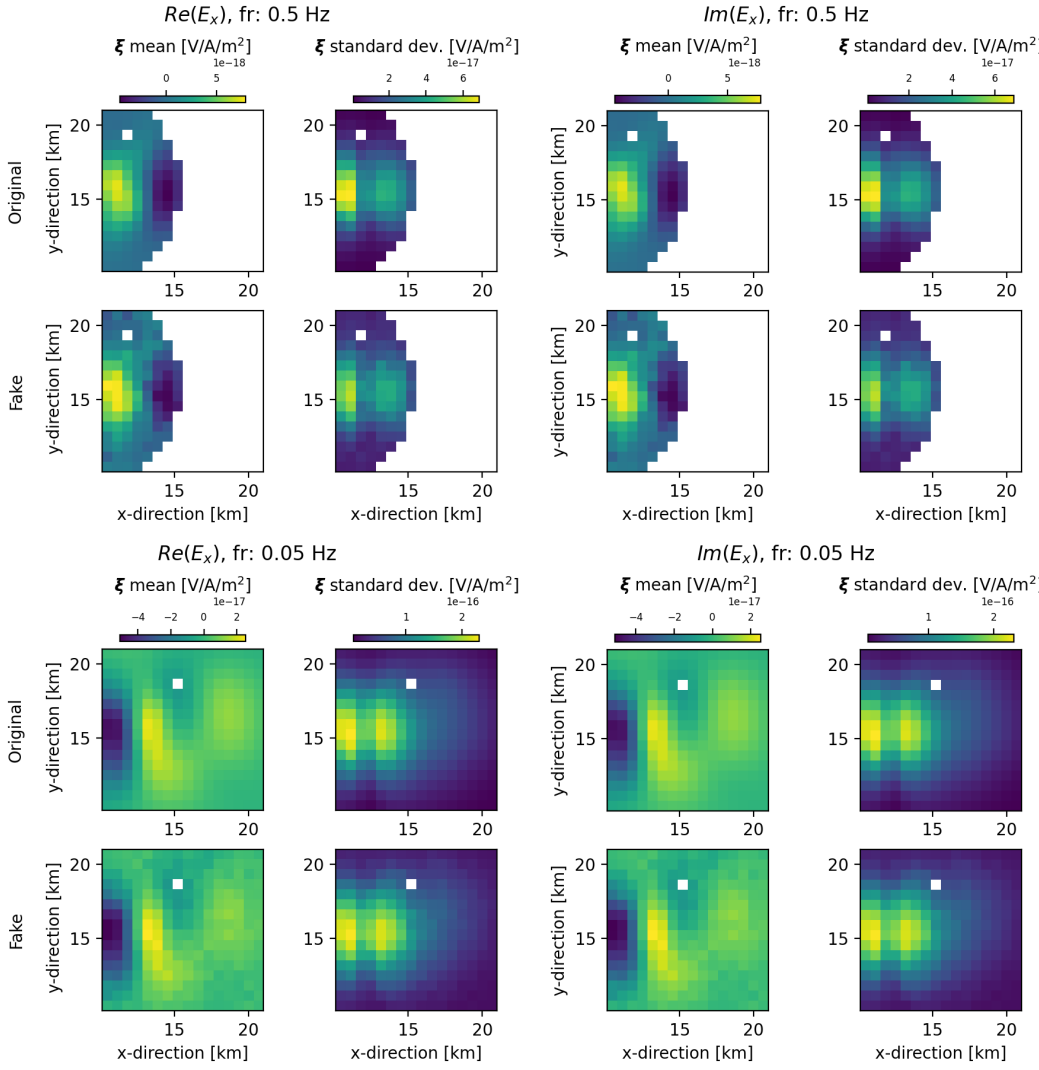

FIGURE 3 Comparisons of the correction ($\boldsymbol{\xi}$) statistics obtained from (1) the training database (rows labeled "Original") and (2) a set of 18,890 synthetic realizations generated by the trained neural network (rows labeled "Fake"). Panels are organized in 2×2 groups. In each group, the title indicates the data channel (electric-field component in x or y, real or imaginary part, and frequency); the columns show the $\boldsymbol{\xi}$ mean (over the database samples) and $\boldsymbol{\xi}$ standard deviation (over the database samples); and the rows correspond to the "Original" and "Fake" databases. Within each plot, the horizontal axis represents the receiver x-position, while the vertical axis represents the receiver y-position. The close agreement between the statistical metrics of both datasets demonstrates that the generative model successfully captures the distribution of the training data. For illustration, only four of the twelve available data channels are shown.

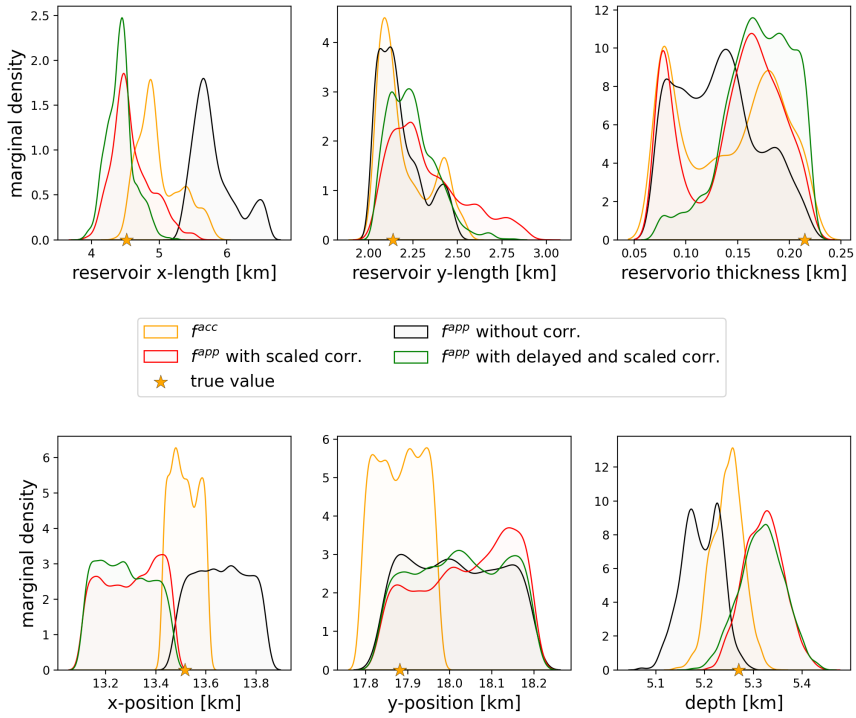

FIGURE 4 Marginal posterior density functions of the reservoir parameters obtained in the synthetic inversion. The top row displays the inferred dimensions in the x-, y-, and z-direction, while the bottom row shows the estimated position coordinates of the anomaly centroid in x, y, and depth relative to sea level. Four inversion scenarios are illustrated: using the approximate forward computation (f^{app}) without correction, with scaled correction, with delayed and scaled correction, and using the accurate forward computation (f^{acc}) (see Table 2 for distribution statistics).

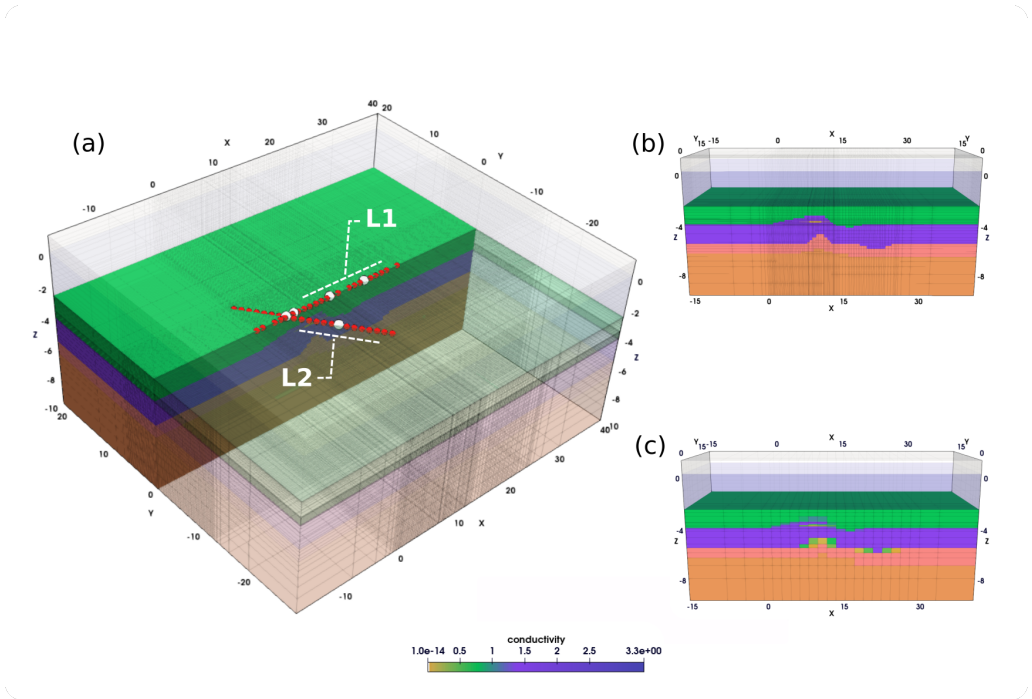

FIGURE 5 Data acquisition design and computational domain for the inversion process for the marine CSEM experiment in Southern Brazil. a) Acquisition lines L1 and L2, including the receiver locations (red dots) and source positions (white dots), as well as the 3D Cartesian computational domain employed for both the observed data and the forward computations (accurate and approximate). b) Illustration of the fine discretization ($114 \times 80 \times 60$ elements) used in the accurate forward computation, highlighting the topographic variations of the stratified layers and the lenticular reservoir. c) Coarse discretization ($44 \times 32 \times 30$ elements) applied in the approximate forward computation, showing the resulting adjustments in the conductivity distribution due to mesh coarsening strategy. The conductivity color bar is in siemens per meter and Cartesian axes in kilometers.

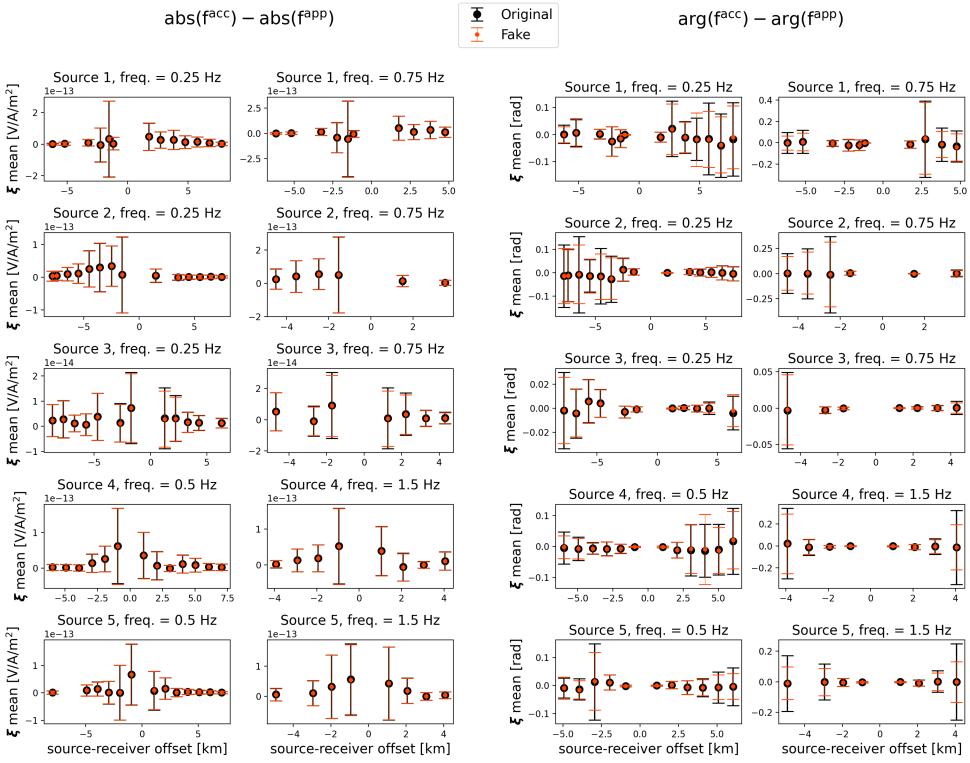

FIGURE 6 Comparison between statistical metrics from (1) the "Original" database used for training (in black) and (2) a "Fake" database generated by the trained neural network (in red). Both databases contain 19,886 samples $\boldsymbol{\xi}$. The first two columns display amplitude values (amplitude differences between the accurate and approximate forward computations, $\mathrm{abs}(\mathrm{f}^{\mathrm{acc}}) - \mathrm{abs}(\mathrm{f}^{\mathrm{app}})$), while the last two columns show phase values (phase differences between the accurate and approximate forward computations, $\arg(\mathrm{f}^{\mathrm{acc}}) - \arg(\mathrm{f}^{\mathrm{app}})$). In each panel, the mean (dots) and standard deviation (error bars) of each database are plotted as a function of the source–receiver offset on the horizontal axis, and either amplitude or phase on the vertical axis, depending on the column. The corresponding source and frequency are indicated in the panel titles. An excellent agreement is observed between the statistical metrics for each component, indicating the generative model's ability to reproduce the underlying data distribution.

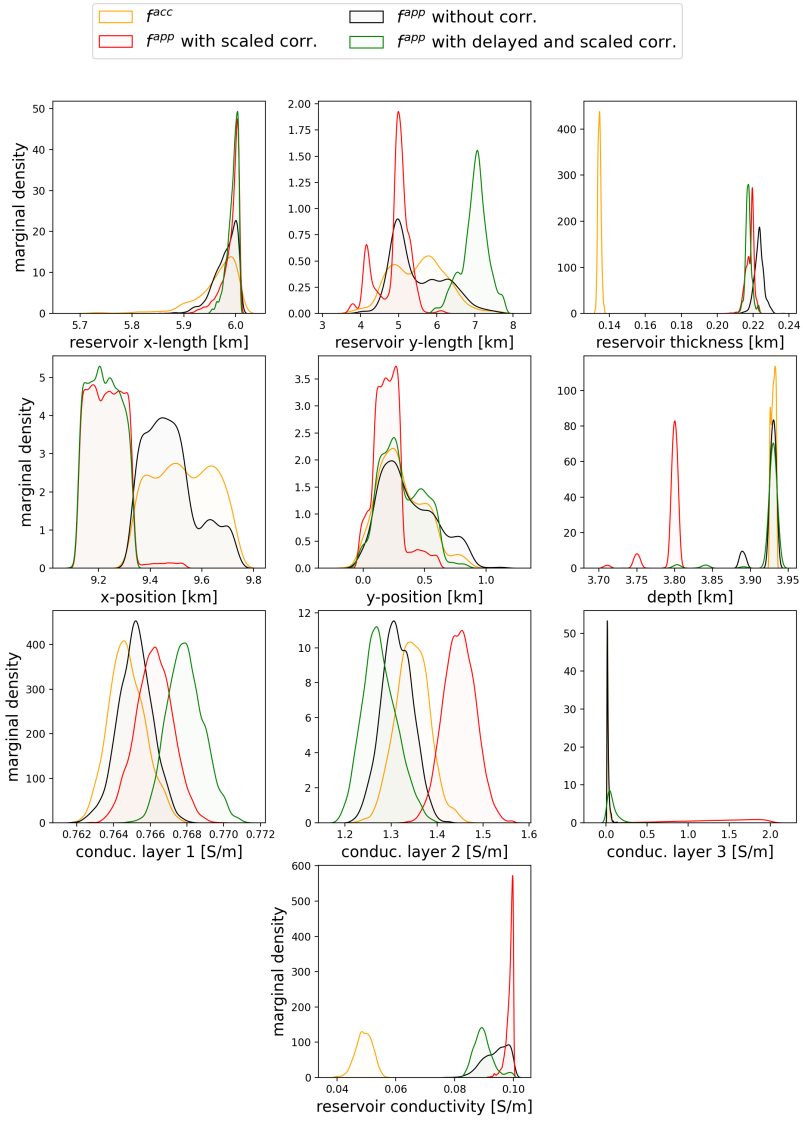

FIGURE 7 Marginal posterior density functions of the ten subsurface parameters obtained in the data field inversion. Four inversion cases: using the approximate forward computation (f^{app}) without correction, with scaled correction, with delayed and scaled correction, and using the accurate forward computation (f^{acc}) (see Table 7 for distribution statistics). The top row displays the parameters associated with the reservoir dimensions in the x-, y-, and z-direction. The second row shows the reservoir position parameters in x-, y-direction, and depth relative to sea level. The third row corresponds to the conductivity values of the three inverted subsurface layers, and the bottom row depicts the conductivity of the reservoir. These last four parameters were inverted using a base-10 logarithmic scale but are shown here in terms of actual conductivity values.

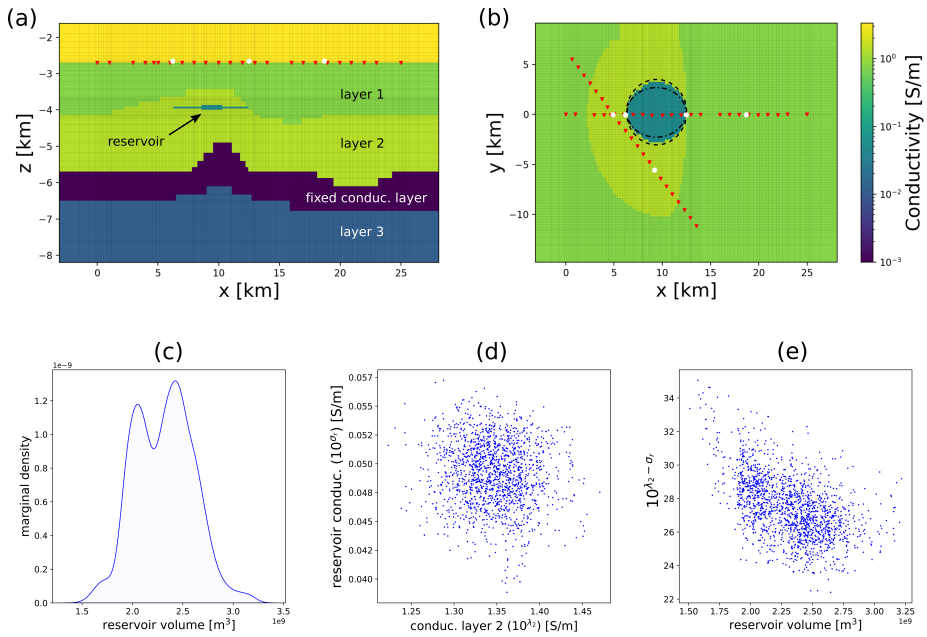

FIGURE 8 Most likely model parameters and variability of reservoir geometry. (a) Plan view in the xz plane along line L1, and (b) plan view in the xy plane at the reservoir depth showing the most likely model parameters. Red triangles and white circles denote receiver and source locations, respectively. The dashed line represents the mean reservoir dimensions plus one standard deviation, while the dash-dotted line represents the mean dimensions minus one standard deviation. (c) Marginal posterior density function of the reservoir volume. (d) Scatter plot between the conductivity of layer 2 (10^{λ_2}) and the reservoir conductivity (10^{σ_r}). (e) Scatter plot between the reservoir volume and the reservoir conductivity contrast ($10^{\lambda_2 - \sigma_r}$).

Appendix A: Mesh coarsening approach

1. **Definition of grids.** We define two physical domains $\Omega^c \subseteq \Omega^f \subseteq \mathbb{R}^3$ corresponding to the coarse and fine grids, respectively. The coarse grid is given by the partition $V_i^c,\ i = 1, \ldots, n_c$, where $n_c = n_x^c \times n_y^c \times n_z^c$ is the total number of elements in the grid, and n_x^c, n_y^c, and n_z^c denote the number of elements in the x-, y-, and z-direction of the domain, respectively. Similarly, the fine grid is given by the partition $V_j^f,\ j = 1, \ldots, n_f$, where $n_f = n_x^f \times n_y^f \times n_z^f$ is the total number of elements in the fine grid, with $n_f > n_c$. The cell volumes are denoted by $|V_i^c|$ and $|V_j^f|$. The conductivity on the fine grid is given by the vector $\sigma^f \in \mathbb{R}^{n_f}$ with components σ_j^f. We aim to define a *coarsening* operation $C(\cdot)$ such that $\sigma^c = C(\sigma^f) \in \mathbb{R}^{n_c}$.
2. **Superposition and fraction.** We first superimpose the grids to compute, for each pair of cells V_i^c and V_j^f, their intersection fraction

$$\theta_{ij} = \frac{|V_i^c \cap V_j^f|}{|V_i^c|}. \tag{5.1}$$

In practice, only q_i values are nonzero for each i, corresponding to the fine cells overlapping with the coarse cell. For each coarse cell V_i^c, we define the index set of intersecting fine cells as

$$T_i = \{j \in \{1, \ldots, n_f\} \mid \theta_{ij} > 0\}, \quad q_i = |T_i|. \tag{5.2}$$

Each $j \in T_i$ has conductivity σ_j^f and relative volume fraction θ_{ij}, satisfying $\sum_{j \in T_i} \theta_{ij} = 1$.

3. **Grouping repeated values.** From T_i, we define the subset $U_i \subseteq T_i$ containing only the indices associated with distinct conductivity values, so that $|U_i| = r \leq q_i$. This subset U_i represents the unique conductivity classes present in V_i^c and forms the basis for calculating the aggregated volume fractions associated with each distinct

value. For each unique class $k = 1, \ldots, r$, we define the aggregated fraction

$$\iota_{i,k} = \sum_{j \in H_{i,k}} \theta_{i,j}, \tag{5.3}$$

where $H_{i,k} \subseteq T_i$ is the set of fine cells whose conductivity belongs to the k-th unique class. Thus, we obtain r representative conductivities $\sigma_{i,k}$ and their corresponding r fractions $\iota_{i,k}$, which summarize the volumetric composition of V_i^{c}.

4. **Definition of effective conductivity.** For each coarse cell V_i^{c} ($i = 1, \ldots, n_c$), we have r unique conductivities $\sigma_{i,1}, \ldots, \sigma_{i,r}$ and their associated volume fractions $\iota_{i,1}, \ldots, \iota_{i,r}$. The effective value σ_i^{c} is estimated as the average of the lower (HS$^-$) and upper (HS$^+$) multi-phase Hashin–Shtrikman bounds (Berryman, 1995):

$$\sigma_i^{\mathrm{c}} = \frac{1}{2}\left(\sigma_{i,\mathrm{HS}^-} + \sigma_{i,\mathrm{HS}^+}\right). \tag{5.4}$$

If we set $\sigma_{i,\mathrm{HS}^-} = \Sigma(\sigma_{\min})$ and $\sigma_{i,\mathrm{HS}^+} = \Sigma(\sigma_{\max})$, with $\sigma_{\min} = \min_k \sigma_{i,k}$ and $\sigma_{\max} = \max_k \sigma_{i,k}$, the bounds can be computed as

$$\Sigma(s) = \left(\sum_{k=1}^{r} \frac{\iota_{i,k}}{\sigma_{i,k} + 2s}\right)^{-1} - 2s, \tag{5.5}$$

where s takes the value $\sigma_{\min}$ or $\sigma_{\max}$ as appropriate.